Bulgarian Academy of Sciences

Institute of Optical Materials and Technologies "Acad. Jordan Malinowski"

SYNOPSIS of

dissertation for the educational and scientific degree "doctor of philosophy"

Professional field 4.1 Physical Sciences

Doctoral program "Electrical, Magnetic, and Optical Properties of Condensed Matter"

Sensors based on spectral polarimetric detection

Petar Kolev

Scientific supervisor: **Prof. Georgi Dyankov, PhD**

Sofia, 2025

The dissertation was discussed and approved for defense at a meeting of the Colloquium of the Institute of Optical Materials and Technologies - Bulgarian Academy of Sciences (IOMT-BAS), held on …… ...

The dissertation consists of a declaration of originality, a list of basic symbols and abbreviations, 3 chapters, including the overview chapter, main contributions, a list of publications related to the dissertation, a list of citations of the author's publications, and a bibliography of sources. The dissertation contains 106 pages, 64 figures, and 11 tables.

The defense of the dissertation will take place on ……. at ……. in room ….. of block 109 of the IOMT-BAS in an open session of the scientific jury composed of: …

ABREVIATIONS

MCSP - Method of Channeled Spectral Polarimetry

CSP – Channeled Spectrum Polarimeter

SOP – State of Polarization

SPR - Surface Plasmon Resonance

LLOD - Lower Limit of Detection

ULOD - Upper Limit of Detection

LOD - Limit of Detection

LOQ - Limit of Quantity measurement

SNR - Signal to Noise Ratio

QF - Quality Factor

FOM - Figure Of Merit

FWHM - Full Width at Half Maximum

RCWA - Rigorous Coupled Wave Analysis

RI - Refractive Index

TM - Transverse Magnetic

TE - Transverse Electric

AOM - Acusto-Optic Modulator

DR - Dynamic Range

PEM - Photo Elastic Modulator

CCD - Charged-Coupled Device

PZT - Piezoelectric Transformer

VIS – Visible spectrum

N-IR - Near-Infra Red spectrum

CMOS - Complementary Metal-Oxide-Semiconductor

BSC - Babinet-Soleil Compensator

MOS – Magneto-Optic sensor

MOM – Magneto Optic Materials

MOE – Magneto-Optic Effect

TEC) – Thermo-Electric Cooler

MSM – Method of Spectral Modulation

OPD – Optical Path Differences

INTRODUCTION

MCSP (Method of Channeled Spectral Polarimetry) is a technique for determining the state of polarization (SOP) within a given spectral range, based on polarization interference that produces amplitude–phase modulation in the spectral domain. By using polarization-modulating optical elements, typically two thick birefringent phase plates (quartz or calcite) with a specific thickness ratio, oriented at a defined azimuthal angle relative to each other, together with a linear polarizer, the amplitude–phase modulation is achieved. The modulated spectrum is analyzed by a spectrometer, and a "single-shot" measurement is recorded. After processing with a Fourier or another numerical algorithm, all Stokes parameters for the examined spectral range are extracted. The Stokes parameters fully determine the state of polarization.

The MCSP is still not widely used in the field of optical sensing. Potential applications include: (1) optical sensors based on Surface Plasmon Resonance (SPR) for gas detection (H2 and other hazardous gases) and for monitoring biomolecular interactions (biosensing); (2) magneto-optic sensors (MOS); (3) material characterization (composition, surface roughness, optical activity, internal structure such as chirality); (4) biomedical optics (investigating tissue structure and properties associated with specific diseases, e.g., carcinomas); (5) pharmaceuticals (measuring the optical activity of drug molecules) and (6) astronomy (object identification and tracking, atmospheric and surface – topological - studies, etc.). In this dissertation, the application of MCSP in SPR-based and MOS sensors is investigated.

SPR is a particularly suitable method for sensor applications due to its exceptional sensitivity to changes in the refractive index of the surrounding medium, its direct and label-free measurement capability, and its ability to monitor processes in real time. The interaction between light and the metal surface leads to the excitation of surface plasmon waves, with the resonance condition being strongly dependent on the properties of the surface. Even minimal changes caused by the adsorption of gas molecules or biological substances result in distinct phase or amplitude variations, making SPR an extremely sensitive optical method for detecting a wide range of reactions.

An additional advantage of SPR lies in its spectral and geometrical versatility—the method can be implemented through a prism, a diffraction grating, or fiber-optic systems, thereby enabling adaptation to diverse applications and facilitating the miniaturization of sensing devices. The capability for phase-based measurement and detection, particularly when SPR is combined with the MCSP, provides enhanced sensitivity and improved noise resistance compared to amplitude-based measurement. As a result, reliable measurements can be achieved even at low concentrations of gases or biological molecules.

MOS are highly sensitive devices based on the Faraday effect, in which the plane of polarization of light rotates as it propagates through a magneto-optic material (MOM) placed in a magnetic field. This phenomenon enables the conversion of magnetic induction into a measurable optical signal that can be recorded with high accuracy and reliability. Owing to their

immunity to electrical noise and their ability to operate under extreme conditions, MOS are widely used in industrial automation, power engineering, medical diagnostics, and scientific research. Their combination of precision, speed, and robustness establishes them as a key technology for modern measurement and control systems.

Although the first reports on the practical implementation of the MCSP date back more than 25 years, issues related to the accuracy and type of algorithms for processing experimental data, design specifics, sources of error, and similar considerations are still being discussed in the specialized literature. These factors are likely the reason why the method is not being widely used in sensing.

The application of the MCSP in SPR sensors would drastically improve parameters such as sensitivity, signal-to-noise ratio, and lower limit of detection, owing to the measurement of the phase difference between the two wave polarizations, p- and s-, at the onset of plasmon resonance. The method is highly promising for use in biosensors based on SPR excited in diffraction gratings - an area of investigation at IOMT - BAS. Diffraction gratings are not typically preferred for SPR excitation, since conventional amplitude detection is less efficient compared to other widely used SPR excitation schemes. Phase detection implemented through MCSP can overcome this limitation. This, together with the significant advantages of SPR in diffraction gratings - namely: (i) excitation of the plasmon wave by both p- and s- polarized light (achieved in the so-called conical mounting of the grating); (ii) the possibility for miniaturization (enabling field-deployable “point-of-care” applications); and (iii) the potential for high-throughput mass fabrication - could make them a leading platform for SPR sensors.

In SPR sensors based on diffraction gratings for hazardous-gas detection, several significant challenges arise. First, the traditionally used amplitude measurement suffers from limited sensitivity - the changes in the intensity of the reflected or diffracted light are often small and difficult to distinguish from noise fluctuations. This results in reduced reliability when measuring low concentrations of gases such as hydrogen, methane, or other toxic substances. Another issue concerns signal stability: amplitude-based measurements are highly dependent on external factors such as fluctuations in the source intensity, mechanical vibrations, or temperature variations, which limit the practical applicability of these sensors in real-world environments. The application of the MCSP offers a solution to these limitations. By measuring the phase difference between the p- and s-polarized components, SPR sensors become significantly more sensitive to small refractive index changes induced by the adsorption of gas molecules on the metal surface of the grating. This enables the detection of concentrations that are unattainable with amplitude-based measurements. Moreover, the measurements become more robust against noise and intensity fluctuations, thereby improving overall accuracy.

In conclusion, the limitations of diffraction-grating-based SPR sensors - namely, lower sensitivity and signal instability - can be overcome through the integration of the MCSP. This approach enables phase-based measurement with high sensitivity and strong noise immunity, making MCSP a key technology for the development of reliable and precise optical sensors.

In the Faraday-effect-based MOS, the primary limitation is temperature instability. The MCSP has the potential to overcome this issue, since under certain conditions it enables direct measurement of the phase difference generated by the Faraday effect, which in turn is independent of temperature.

This determines the **relevance** of the issue of the application of MCSP in various types of optical sensors. The most suitable sensors are those in which the detection process is accompanied by a change in SOP, for example, sensors based on SPR and MOS sensors. Given the main problems for all types of sensors - sensitivity, resistance to external influences, and measurement accuracy, this dissertation examines the extent to which the application of MCSP can solve them.

The CSP method has not been commercialized, and there is no equipment on the market that can perform such measurements. This determined one of the main tasks of the dissertation: to design and fabricate CSP.

These are the grounds for formulating the objective of the dissertation:

Investigation of the applicability and efficiency of the CSP method for different types of sensors.

To achieve this goal, the following tasks were performed:

1. Design and creation of CSP:

- optimization of the parameters of the main structural elements in accordance with the existing measuring equipment.

- Investigating and minimizing sources of error, establishing accuracy and resolution.

2. Experimental determination of phase measurement characteristics:

- high signal-to-noise ratio: achieved through pathogen detection in diffraction-grating-based SPR biosensors;

- high sensitivity through: (i) detection of H2 in diffraction-grating-excited SPR gas sensors; (ii) model experiments performed to determine sensitivity;

- through direct measurement of the phase difference associated with changes in the state of polarization in magneto-optic sensors.

CHAPTER 1: LITERATURE REVIEW

The main type of sensors to which we applied the MCSP are SPR-based sensors. The argument is that when plasmon resonance is excited, a sharp phase difference arises between the s- and p-polarizations, which can be effectively measured by CSP. The review begins with a brief overview of SPR sensors.

Historically, the two main approaches for optical excitation of SPR are: 1) ATR (Attenuated Total Reflection) in prism-based systems, pioneered by Nylander and Liedberg. [1]. The method is used to characterize thin films [2] [3]and bio (chemical) sensors [4] [5] [6]; 2) Diffraction in diffraction grating (grating) based systems, pioneered by Cullen et al. [7], thanks to whom this method is being implemented as an alternative to the prism method [8] [9].

The main parameters describing SPR-based sensors are: sensitivity S, resolution $\Delta\lambda$ (spectral), $\Delta\Theta$ (angular) or $\Delta\varphi$ (phase), depending on the measured quantity, linearity, reproducibility, dynamic range DR (Dynamic Range), lower limit of detection (LLOD), upper

limit of detection (ULOD), limit of quantification (LOQ), signal-to-noise ratio (SNR), quality factor (QF), and figure of merit (FOM) parameter for the overall system. With amplitude (spectral and angular) measurement and prism-excited SPR, we have higher values for the sensitivity, accuracy, and FOM parameters compared to the use of grating-excited SPR.

Siqi Long et al. [10] examine grating excited SPR sensors using commercial BD-R, CD-R, and lithographically fabricated gratings, and investigate the relationship between the period Λ and sensitivity S. Due to the lower sensitivity of grating excited SPR sensors, they perform a theoretical analysis of the limiting sensitivity, which would lead to methods for designing grating excited SPR sensors to achieve maximum sensitivity. The analysis shows that grating with the largest possible period Λ and angle of incidence $\theta \approx 90^0$ should be used to achieve maximum sensitivity for a given measured resonance wavelength λ_{res}, as with an increase in λ_{res}, the maximum sensitivity S_{max} also increases.

They [10] establish that the theoretical $\theta \approx 90^0$ will weaken the absorption peak, experimentally establishing that at $\theta = 55^0$ optimal SPR parameters are obtained. The parameters they achieve are: 1) BD-R (grating parameters – sinusoidal profile, period $\Lambda = 314\ nm$, grating depth $d_G = 20\ nm$, Ag film $\delta_{\mathrm{Ag}} = 50$ nm deposited on the grating profile) – diffraction order $m = 1$, normalized reflection $R_{norm} = \frac{R_{max_y}}{R_{min_y}} = 70\ \%$, $FWHM = 10\ nm$, $S = 319.96\ nm/RIU$, $FOM = 32.00$, spectral resolution $\Delta\lambda = 0.2264\ nm$, RI (Refractive Index) resolution $\Delta n = \Delta\lambda/S = 0.00071\ RIU$; 2) CD-R (grating parameters – profile – Gaussian-shaped peak with flat base, $\Lambda = 1470\ nm$, $d_G = 119\ nm$, the half-width of the grating peak is $FWHM_G = 452\ nm$) - $R_{norm} = 60\ \%$ (the reason for the low value is that the metal layer separated from the CD-R is not smooth enough, and the depth $d_G = 119\ nm$ is slightly too large to excite the SPR), $FWHM = 42\ nm$, $S = 1477.74\ nm/RIU$, $FOM = 35.18$, $\Delta\lambda = 0.5760\ nm$ (the reason for the lower value compared to BD-R is the non-ideal surface profile of the grating); 3) grating manufactured using a photolithographic method (grating parameters - profile - rectangular with a working cycle of 1:1, $\Lambda = 6733\ nm$, $d_G = 202\ nm$) – $m = 3$, $R_{norm} = 4\ \%$, $FWHM = 61\ nm$, $S = 2077.26\ nm/RIU$, $FOM = 34.05$, $\Delta\lambda = 2.7220\ nm$ (the reasons for the lower value compared to those for BD-R and CD-R are: i) the use of $m=3$; ii) the relatively low resolution of the infrared spectrometer used by them); $\Delta n = 0.00131\ RIU$ (to increase the value of Δn, it is necessary to work with $m = 1$ and optimize the structural parameter of the grating).

It is necessary to review and briefly analyze the achievements to date in the field of grating-based SPR sensors in terms of increasing their sensitivity. Metal gratings can be produced by laser interference lithography [11], thermal nano printing [12] [13], wet etching [14], and methods based on optical discs [15] [16]. One approach to achieving higher sensitivity is by increasing Λ [17] [18]. Xuan Dou et al. [19] numerically achieve $S = 1610\ nm/RIU$ using grating with $\Lambda = 1600\ nm$. Y. Lang et al. [20] use a resonator array of Au nano rings as a sensor chip, achieving: $FOM = 513\ nm/RIU$ and $\Delta n = 1.3219\ RIU$.

Grating-based SPR sensors have great potential to meet the requirements for applications in biosensors, their main advantage being miniaturization, which in turn contributes to the implementation of the so-called "point of care". In this regard, Sharma and Pandey [21] numerically model an Al2O3 grating-based SPR sensor for measuring the concentration of hemoglobin in human blood. The effects of the parameters of the grating, the

metal, and the thickness of the dielectric film on the performance of this type of sensor are also investigated.

The advantages of grating-based SPR are: 1) miniaturization; 2) adjustable rotation angle; 3) integration into a "lab on a chip"; 4) application in biosensors without the use of labeling. Despite the listed advantages, amplitude measurement cannot achieve sufficiently high accuracy and sensitivity compared to a prism-based SPR sensor. This necessitates the application of another measurement method: phase measurement of SPR, in which sensitivity and accuracy are an order of magnitude higher than prism-based SPR and grating-based SPR with amplitude measurement.

Phase measurement of SPR is a method in which the change in the p- polarized component of light is monitored when SPR occurs. Lahav et al. [22] use interpolation in the SPR minimum region, thereby achieving an improved LOD (Limit of Detection). Nelsen et al. [23] developed the first SPR sensor based on an optical heterodyne with a He-Ne laser and an AOM (acousto-optic modulator), achieving $S_{\Delta\varphi} = 5 \cdot 10^{-7}\, RIU$. Shen et al. [24] uses a frequency-stabilized Zeeman laser, achieving $S_{\Delta\varphi} = 1 \cdot 10^{-7}\, RIU$. Kabashin et al. [25] investigated $\Delta\varphi$ and the polarization transformations that occur during SPR, proposing the use of the "phase jump" caused by SPR, significantly improving sensitivity and LOD: $S = 10^5\ °/RIU$, $LOD = 10^{-8} RIU$. In the field of interferometry with spatial phase measurement: Kabashin et al. [26] [27] achieved $LOD = 4 \cdot 10^{-8} RIU$ in gas detection; Yu et al. [28] achieved measurement accuracy of the interference fringes $\Delta\varphi = 3 \cdot 10^{-5} RIU$.

Various approaches are used to improve the parameters of phase measurement SPR sensors: 1) increasing sensitivity by using a combination of graphene with noble metals [29]; 2) expanding the dynamic range *DR* – Ng et al. [30] achieve $DR > 10^{-2} RIU$ and $LOD = 2.2 \cdot 10^{-7} RIU$ using differential spectral interferometry, while Ho et al. [31] [32], applying time modulation of the excitation beam by means of a photoelastic modulator, obtain *DR > 0.06 RIU* and $LOD = 2.89 \cdot 10^{-7} RIU$; 3) improvement of spatial resolution: Somekh et al. [33] developed an interferometric microscopic system, and Gerber et al. [34] used graphene, applying NIR interferometry; 4) portable designs – Sepulveda et al. [35] implement a Mach-Zehnder interferometer in a "lab on a chip", Ahn et al. [36] develop an SPR sensor with optical fiber and waveguide, Liu et al. [37] implement an SPR sensor based on optical fiber-based on a smartphone platform.

There are several advantages of phase measurement SPR sensors over conventional SPR sensors based on intensity, angular, and spectral measurement: 1) greater sensitivity; 2) a self-referencing method; 3) higher SNR.

The phase measurement SPR method can be further optimized by using various optical analysis techniques and subsequent signal processing. An extremely promising approach in this direction is the use of the MCSP method. The latter is considered in this dissertation not only as a means of improving phase measurement of the SPR in a biosensor for the detection of *Helicobacter Pylori* and a gas (hydrogen) sensor, but also applied in MOS, where, thanks to the complete characterization of SOP, the rotation of the Faraday plane under the influence of an external magnetic field can be determined directly, with high accuracy and sensitivity, and MOS is not affected by changes in the ambient temperature.

Oka et al. [38] describes the principle of MCSP in its most complete form for the first time. The main advantages of the method are: 1) No mechanically moving components for polarization control or active components for polarization modulation are used to measure the spectrally resolved SOP; 2) The influence of vibrations and temperature is minimized; 3) All spectrally dependent parameters of Stokes $S_0(\sigma)$, $S_1(\sigma)$, $S_2(\sigma)$ and $S_3(\sigma)$ are determined by only one spectrum $P(\sigma)$; 4) Unlike conventional polarimeters, it is not necessary to repeat the spectrum measurement for different optical settings for polarization analysis; 5) Higher values of: *SNR*, *DR*, and *LOD*.

CHAPTER 2: DESIGN OF A CHANNELED POLARIMETER

2.1 Design of the CSP. Experimental setup

This chapter discusses the optimization procedure, considering the parameters of existing measuring equipment, and the construction of the CSP to achieve maximum phase shift.

2.1.1 Calculation of phase plate thicknesses

The thicker the phase plates, the higher the frequency of the spectral modulation. However, its registration depends on the resolution of the spectrometer.

Task: Spectral resolution of the modulations with the highest spectral frequency.

To accomplish the task defined above, it is necessary to calculate and optimize the thicknesses and thickness ratios of the phase plates in accordance with the spectral resolution of the spectrometer.

A schematic representation of the experimental setup is shown in Figure 2. 1.

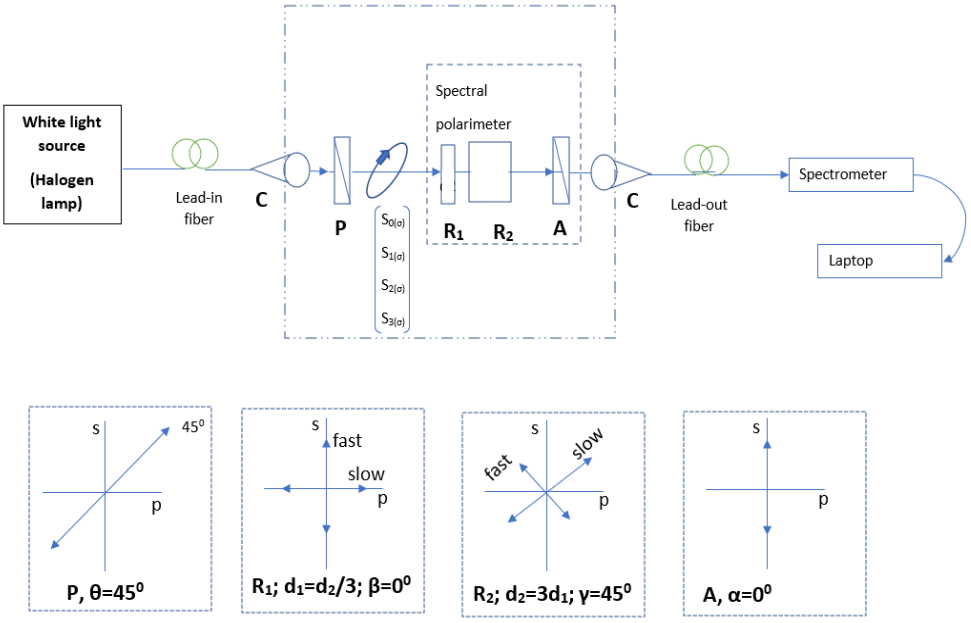

Figure 2. 1 Schematic representation of the experimental setup.

Source of polychromatic light (halogen lamp); R_1, R_2: double-refracting phase plates made of quartz; s-, p-: polarization planes; fast, slow: fast and slow optical axes of the quartz

crystal plates; d - plate thickness; C – collimator. Polarizers – Glan-Thompson, extinction coefficient 10^4. Spectrometer: Ocean Optics SpectraSuit USB2000 or AvaSpec – ULS2048CL-EVO.

Using the algorithm described in detail by N. Hagen [39], the correct thicknesses of the phase retarders were calculated and selected, considering the parameters of the spectrometer.

OPD in one channel: half the range in OPD divided by the number of channels in the Fourier domain (channel width).

OPD range: reciprocal value of the spectrometer's root mean square resolution.

OPD half-bandwidth: due to symmetry in the Fourier domain, this is half the usable bandwidth.

Delay caused by the thin delay line: (in terms of OPD) a function of the usable half-bandwidth in OPD and the number of channels.

Allowable OPD error: error in the positions of the OPD channels with an allowable maximum amplitude error across the entire spectral range <1%.

Delay line thickness error: this is the tolerance at which the allowable OPD error is not exceeded.

• **Calculation results for AvaSpec – ULS2048CL-EVO are presented in Table 2. 1**:

Table 2. 1

Spectrometer resolution: R_λ [nm]		1 nm - specification of the resolution published by Avantes					
		OPD range / number of channels: <= [-]	OPD range [µm]	OPD half range [µm]	Delay caused by the thin retarder d1 [µm]	Thickness of the retarder d1 [mm]	Thickness of the retarder d2 [mm]
Thickness ratio	d2=2*d1 (7 channels in OPD)	70.7	308.0	154.0	43.971	4.397	8.8
	d2=3*d1 (9 channels in OPD)	55.0	308.0	154.0	34.200	3.420	10.3

- **Calculation results for Ocean Optics SpectraSuit USB2000 are presented in** Table 2. 2

Table 2. 2

Spectrometer resolution: R_λ [nm]		1.4 nm - specification of the resolution published by Ocean Optics					
		OPD range / number of channels: <= [-]	OPD range [µm]	OPD half range [µm]	Delay caused by the thin retarder d1 [µm]	Thickness of the retarder d1 [mm]	Thickness of the retarder d2 [mm]
Thickness ratio	d2=2*d1 (7 channels in OPD)	70.2	251.0	126.0	35.805	3.580	7.161
	d2=3*d1 (9 channels in OPD)	54.6	251.0	126.0	27.848	2.785	8.354

Conclusion: Retarders have been manufactured with calculated thicknesses and thickness ratios at which the highest frequency modulations are spectrally resolved. Two variants of phase retarders: with a thickness ratio of 1:2 ($R_1 = 4.4$ mm : $R_2 = 8.8$ *mm*) and with a thickness ratio of 1:3 ($R_1 = 3.4$ *mm* : $R_2 = 10.2$ *mm*) were manufactured using the values obtained from the calculation with the AvaSpec-ULS2048 -CL-EVO spectrometer, which has a higher spectral resolution (we chose to work with what is specified in the official documentation, i.e. 1 nm) compared to that of the Ocean Optics SpectraSuit USB2000 (1.4 nm).

2.1.2 Construction of the experimental setup

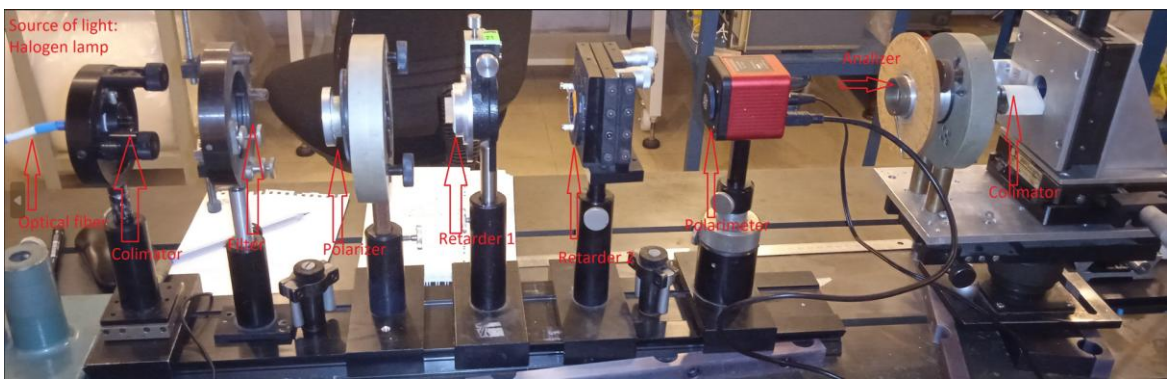

Figure 2. 2 Real laboratory setup – variant 1

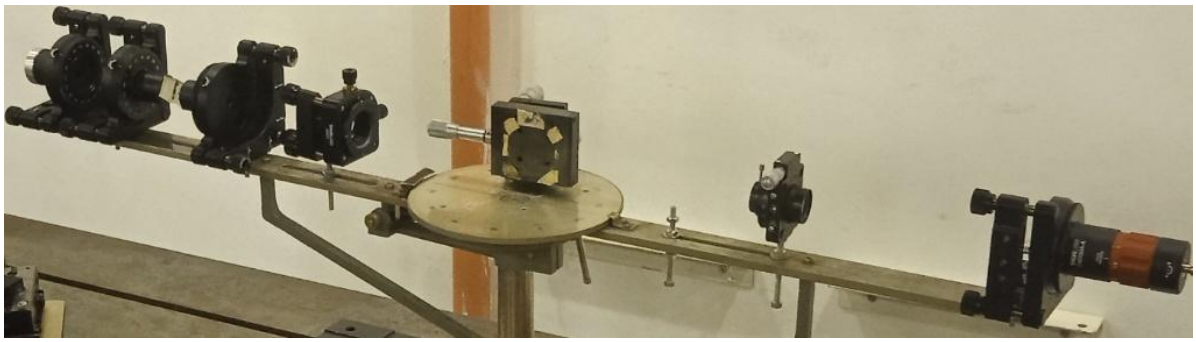

Figure 2. 3 Real laboratory setup – variant 2

Figure 2. 2 and Figure 2. 3 show the developed variants of the experimental setup, while Figure 2. 4 shows only the CSP for variant 2.

Figure 2. 4 CSP (consisting of retarder R_1, retarder R_2, and analyzer A)

Once an experimental setup has been constructed, the next step is to correctly orient the optical elements in the system. This is a very important and mandatory condition, which also leads to the definition of the next task.

Task: The Stokes parameters contained in each channel and the central position of each channel can be compromised by systematic errors inherent in the CSP. Therefore, precise orientation of all optical elements in the system is required.

To solve this problem, we apply two different techniques for orienting the optical components (Section 2.1.3.1 and Section 2.1.3.2 of the dissertation).

2.1.3 Orientation of optical elements

2.1.3.1 Polarimetric orientation

This orientation technique is applied using the setup shown in Figure 2. 5 (light source: He-Ne (632.8 nm), commercial polarimeter Thorlabs PAX 1000 VIS).

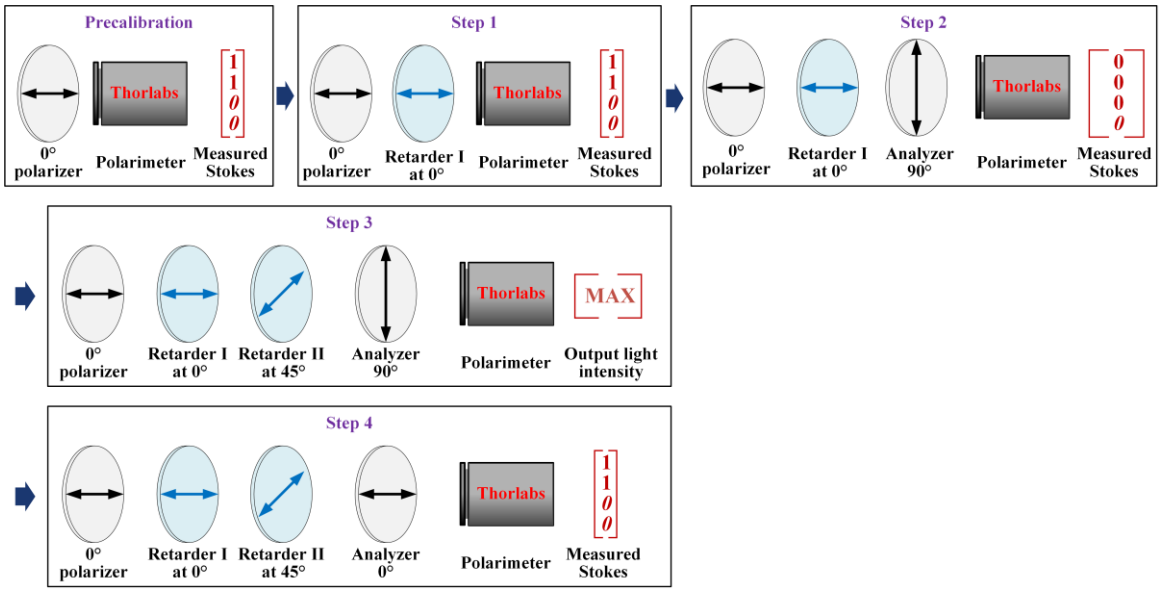

Figure 2. 5 Calibration procedure of the CSP – polarimetric orientation of components.

2.1.3.2 Polarimetric-spectral orientation

The procedure and settings for the entire calibration are shown in Figure 2. 6. It is performed using the experimental setup shown in Figure 2. 3, using two separate light sources: He-Ne (632.8 nm) or halogen lamp (Ocean Optics HL-2000). A commercial Thorlabs PAX 1000 VIS polarimeter is used for polarimetric control. An AvaSpec-ULS2048-CL-EVO spectrometer is used for spectral control.

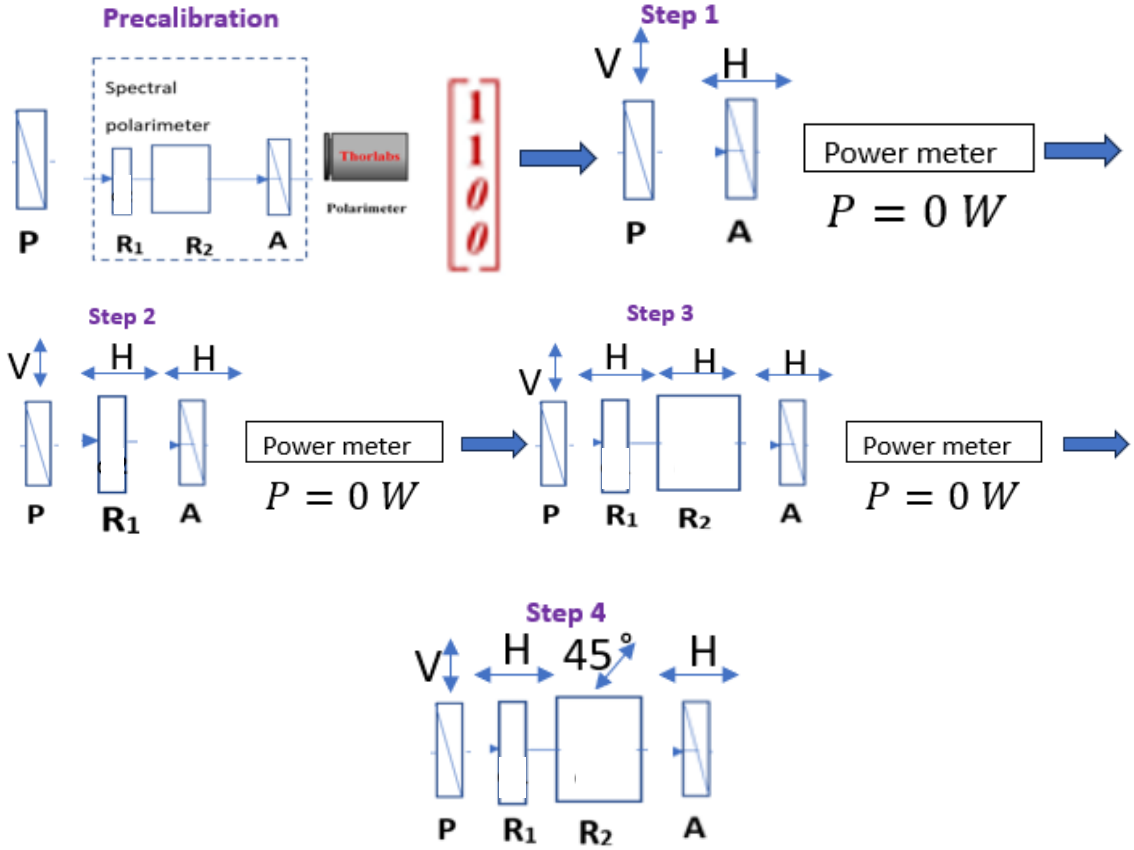

Figure 2. 6 Calibration procedure of the CSP: polarimetric-spectral orientation of the components.

2.1.4 Experimental verification: selection of phase plate thicknesses

A monochromatic source of 632.8 nm – He-Ne laser and Thorlabs polarimeter are used, in which the input analyzer is polarimetrically oriented, giving us a known SOP for this λ. In place of He – Ne, a halogen lamp is placed, the light from which passes through the CSP, the signal is received by the spectrometer, and we obtain the so-called channeled spectrum, which, after applying Fourier processing, we must extract the SOP for the entire measured spectral range (in this case from 500 to 800 nm). Phase retarders with a thickness ratio of 1:3 ($R_1 = 3.4\ mm : R_2 = 10.2\ mm$) are used. Experimental verification establishes that after applying the Fourier algorithm, the Stokes parameters demodulated after CSP coincide with good accuracy with the initially set values of the known input polarization at a wavelength of 632.8 nm, with differences only in the $\frac{S_2}{S_0} \neq 1$ parameter, which is probably due to the insufficiently high degree of polarization (which is a factor of the entire system). Another factor is the fluctuation of the orientation of the fast axes across the thickness of the crystal, due to inhomogeneities in the crystalline structure of the quartz crystal (a change in the orientation of the crystal lattice).

This requires checking the possible orientation options for the retarders, where we have maximum correspondence between the Stokes parameters of the incoming polarization and those after processing with the Fourier algorithm. The latter assumption requires us to conduct additional experimental tests to determine the fast axes of both quartz retarders, which leads to the definition of the following task.

Task: Minimizing the error in the orientation of the phase retarders.

2.1.5 Determination of the fast axes of the two phase retarders

The precise orientation of all optical components is extremely important for achieving high measurement accuracy. The fast axes of the two phase retarders were oriented (using a Thorlabs polarimeter at $\lambda = 632.8\ nm$ – He-Ne laser) for the following plate thicknesses and arrangements (Table 2. 3). Table 2. 4 presents data only for the orientation of the R3.4 and R10.2 phase retarders.

Table 2. 3

d1:d2=1:3	**d1:d2=3:1**
R3.4_↔_R10.2_45˚	R10.2_↔_R3.4_45˚
d1:d2=1:2	**d1:d2=2:1**
R4.4_↔_R8.8_45˚	R8.8_↔_R4.4_45˚

Table 2. 4

Var.	R3.4		R10.2		Input polarization (S_1/S_0, S_2/S_0 , S_3/S_0) - He-Ne	
	Angle of the holder	Polarimetric orientation	Angle of the holder	Polarimetric orientation		
3	60^0	**H**	312^0	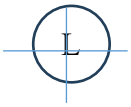	S_1/S_0 =0.12; S_2/S_0 =0.37; S_3/S_0 =0.92	Ref. in. pol. 45^0 linear/ – peaks 0,1,2 In. elip. pol. – peaks 0,1,3 S1=0.19; S2=0.18; S3=0.68 Ref. in. pol. 45^0 linear/ – peaks 0,1,3 In. elip. pol. – peaks 0,1,3 S1=0.19; S2=0.19; S3=0.64

Conclusions: The fast axes of the phase plates are determined (Var. 3 Table 2. 4, where the best match between the measured SOP from the Thorlabs polarimeter and the demodulated SOP at the output after the CSP is achieved; the other variants are presented in the dissertation).

2.1.6 Experimental verification of the orientation of the optical elements and the Fourier algorithm

To verify the correctness of the results obtained in Section 2.1.5, it is necessary to determine the Stokes parameters at the input of the polarimetric system and at any elliptical input polarization, using again the configuration of the R3.4 and R10.2 plate set. When checking with an input polarization with a Stokes vector $[1, 0.12, 0.37, 0.92]^T$ at 632.8 nm, we obtain a good match between the Stokes parameters at the input and those after processing with the algorithm, with an accuracy of $\leq 10\ \%$. The accuracy is determined by: 1) the degree of collimation due to the degree of plane parallelism of the wave fronts (chromatic and spherical aberration); 2) DOP (Degree of Polarization); and 3) parasitic reflections from the retarder planes.

2.1.7 Comparison of the effectiveness of the two phase plate configurations: *R3.4* and *R10.2* versus *R4.4* and *R8.8*, in phase measurement of SPR with CSP

2.1.7.1 Configuration *R4.4* and *R8.8*

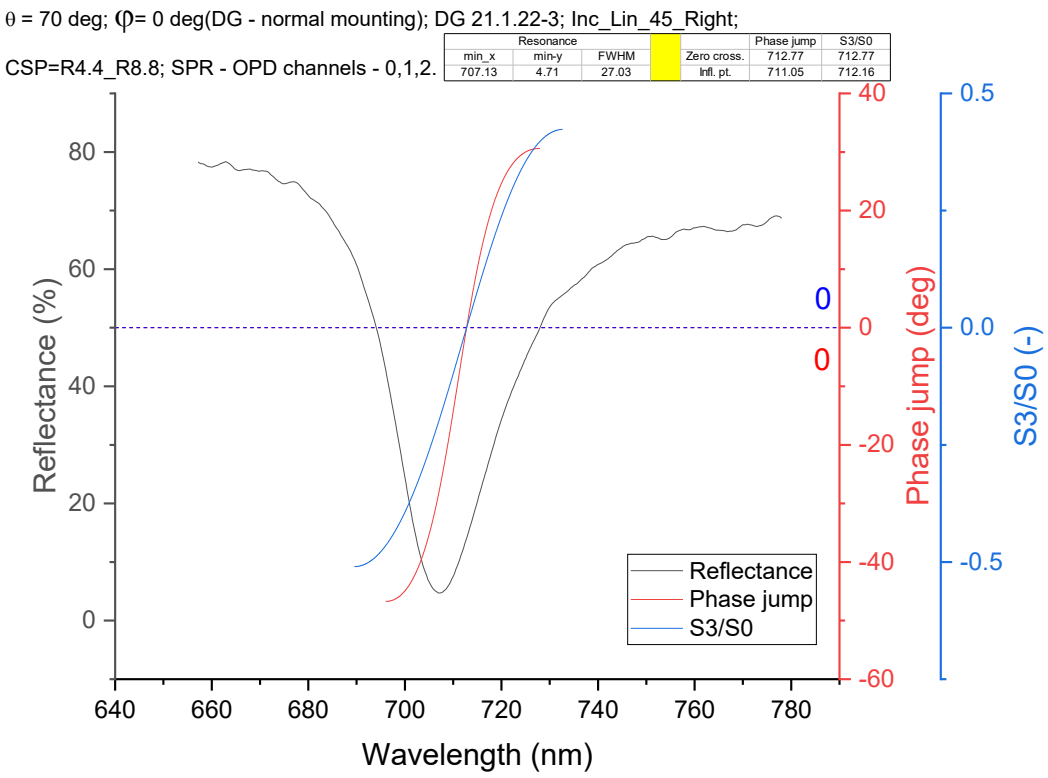

Figure 2. 7 Measurement of SPR - resonance minimum, phase jump, and S_3/S_0 with R4.4 and R8.8.

2.1.7.2 Configuration *R3.4* and *R10.2*

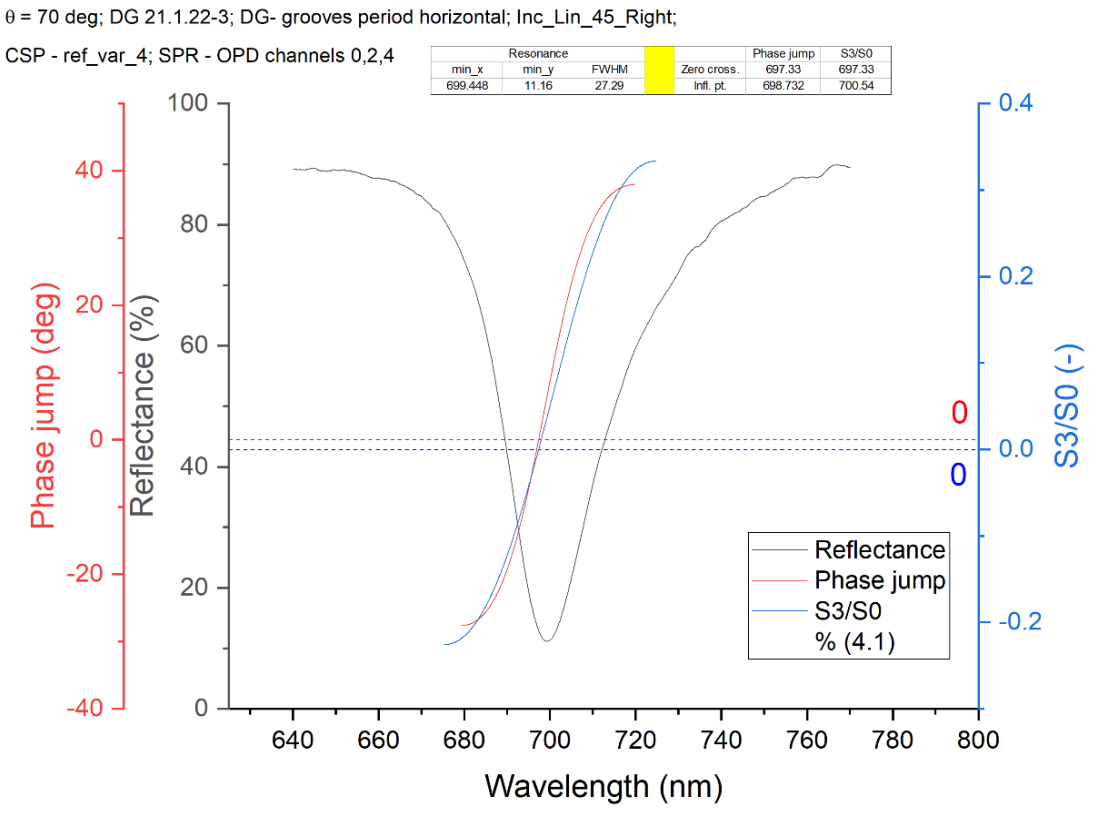

Figure 2. 8 Measurement of SPR - resonance minimum, phase jump, and S_3/S_0 with R3.4 and R10.2.

2.1.7.3 Analysis of results

In both configurations are obtained:

• sufficiently high amplitude-phase modulation in the spectral domain.

• The positioning and number of channels in the Fourier domain also corresponded to expectations [40].

• SPR meaurement is also successful (Figure 2. 7 and Figure 2. 8): the polarimetric parameters S_3/S_0 and phase jump (inflection point and zero crossing) coincide in spectral position with the minimum of resonance.

• The slope of the phase jump is steep enough to ensure high sensitivity and accuracy of SPR measurement.

Conclusion: The *1 : 3* (*R3.4 : R10.2*) phase plate configuration offers higher spectral resolution in each channel, as there are 9 channels, compared to the 1 : 2 (*R4.4 : R8.8*) configuration, which has 7 channels. With *1 : 3*, we have an additional channel containing information about the normalized S_2 and S_3, allowing for more accurate calibration of the CSP, which leads to more accurate extraction of the Stokes parameters.

CHAPTER 3: SENSORS BASED ON SPECTRAL POLARIMETRIC DETECTION

Phase measurement performed by MCSP aims to solve the main problems of sensors by providing higher detection sensitivity, higher SNR, and, accordingly, lower LOD. This motivated us to develop CSP and take advantage of its benefits, mentioned in Section 1.3.1 of the dissertation, by applying it to the detection of various quantities. In this chapter, we investigate the extent to which the developed CSP meets expectations through studies conducted with it on three types of sensors, two of which are grating based SPR sensors:

- biosensor;

- gas sensor;

- magnetic field sensor.

3.1 Biosensor: detection of *Helicobacter pylori* bacteria

A disadvantage of grating based SPR sensors is that light passes through the analyte when detecting the interaction under study, which leads to scattering of the reflected light and significantly worsens the SNR. The hypothesis that phase measurement of SPR successfully overcomes this disadvantage is the subject of experimental verification in the conducted study. For this purpose, the detection of *H. pylori* was performed in a flow cell by amplitude and phase measurements, and the results were compared.

The development of a biosensor for *H. pylori* is dictated by the socio-economic significance of the infection. More than *90 %* of people infected with *H. pylori* are diagnosed with gastroduodenal ulcer. According to the World Health Organization, *H. pylori* infection causes approximately *75 %* of stomach cancer cases and *5.5 %* of all types of cancer. Therefore, timely diagnosis of the infection is imperative.

In [41], a direct method for detecting *H. pylori* was reported, based on the binding reaction between *BabA*, the protein that builds the bacterial cell membrane, and the blood antigen *Levisb*

(*Leb*). The experiment presented uses the same recognition reaction, with *Leb* being the bioreceptor immobilized on a gold-plated diffraction grating, as shown in Figure 3. 1.

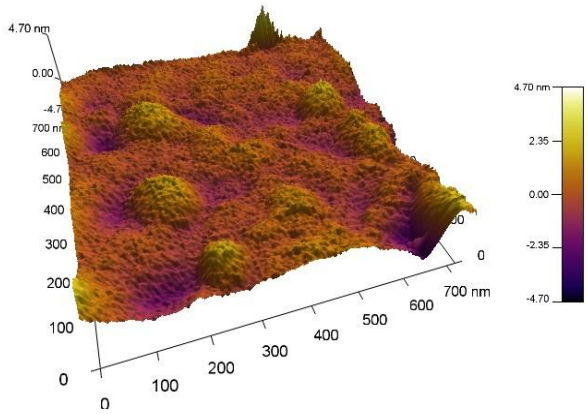

Figure 3. 1 AFM image of immobilized Leb on the diffraction grating

The procedure for preparing bacterial suspensions does not differ from that described in [41]. There are two differences with [41]: incubation is performed in a flow cell (Figure 3. 2) and the measurement of the SPR after incubation/fixation of the bacteria on the biochip (Figure 3. 3) is performed in phase, in addition to amplitude. The measurement is performed in the flow cell. One of its channels is treated with deionized water and serves to measure the reference resonance, while the other is treated with bacterial suspension and measures the signal resonance. During the measurements, the light passes through the analyte, which significantly worsens the SNR.

Figure 3. 2 Flow cell

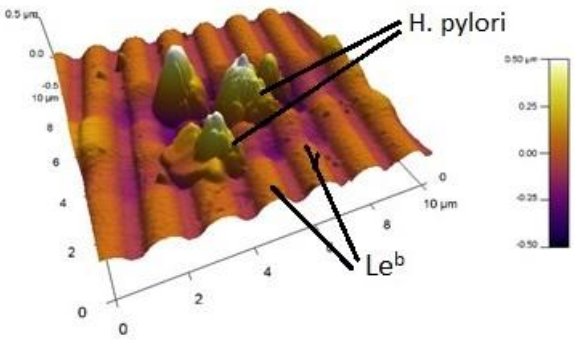

Figure 3. 3 Fixed H. pylori on diffraction grating, resulting from Leb/BabA reaction

The diagram of the experimental setup is shown in Figure 3. 4. The universal diagram for spectral measurement of SPR is shown at the top right; the schematic diagram of the CSP, as described in Section 1.3 of the dissertation, the holder in which the phase plates and the

analyzer are mounted is shown at the bottom right – this holder is placed at position 9 on the goniometer to perform phase measurement. Without it, the SPR is measured by amplitude.

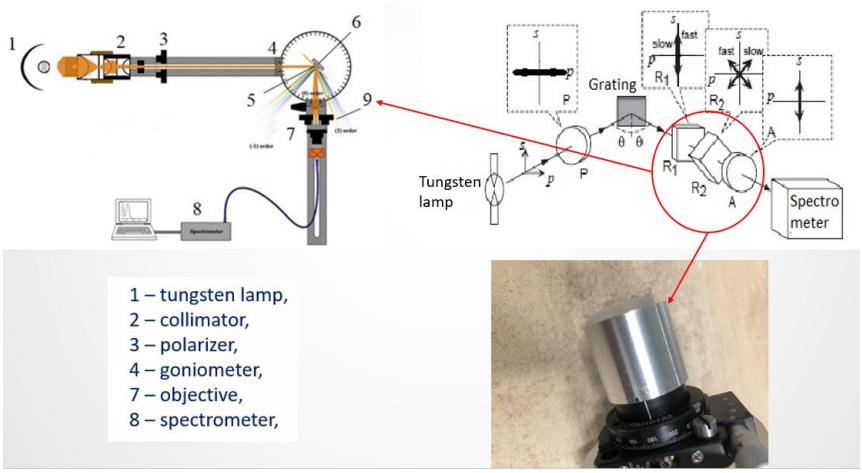

Figure 3. 4 Experimental setup for amplitude/phase measurement of SPR

Figure 3. 5 shows the results of amplitude (solid curves) and phase (dashed curves) measurements of the normalized intensity of reflected light in the zero-diffraction order. SPR occurs at certain wavelengths because of the binding reaction of *H. pylori - Leb* for two different bacterial concentrations (black and red curves). The resonance manifests itself as a smooth and blurred decline in the reflection spectrum during amplitude measurement. Therefore, the accurate determination of the resonance wavelength is difficult and associated with a large error. The dotted curves show the spectral distribution of the phase measured by MCSP, as described in section 1.3 of the dissertation. The spectral dependence of the phase is steep, which is why the resonance position is determined with high accuracy. **This experimental result illustrates the dramatically higher signal-to-noise ratio (SNR) in phase measurement.**

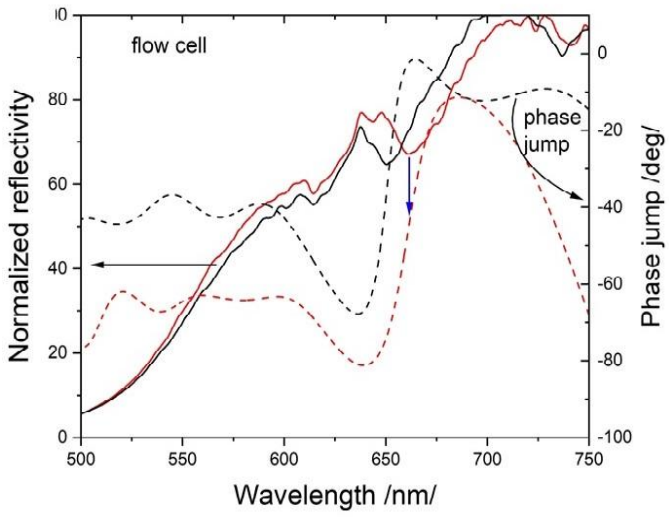

Figure 3. 5 Amplitude (solid lines) and phase (dashed lines) measurement of SPR for detecting BabA/Leb interaction at different bacterial concentrations in a flow cell

The spectral shift shown in Figure 3. 6, caused by the *BabA/Leb* interaction at different bacterial concentrations, is evaluated relative to the reference resonance wavelengths of

untreated biochips. The resonance for each concentration was measured 20 times to establish the measurement error.

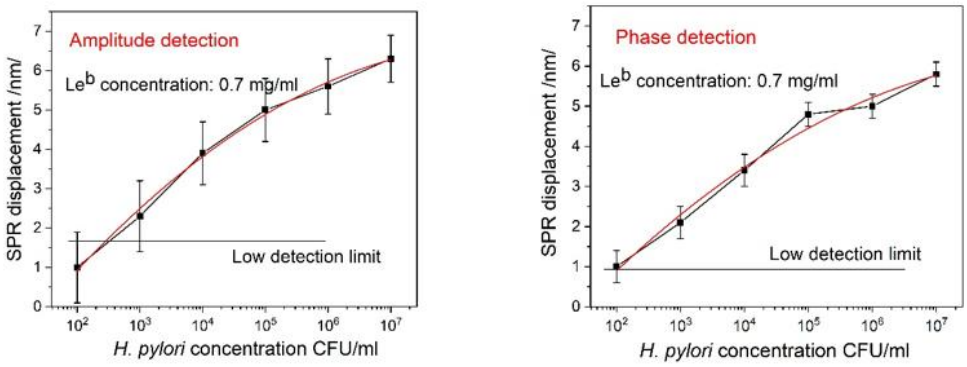

а/ б/

Figure 3. 6 Spectral shift of resonance as a result of the interaction between H. pylori and Leb; a – during amplitude measurement; b – during phase measurement

In amplitude measurement, the spectral position of resonance is found by determining the minimum of the spectral dependence of the normalized intensity of the reflected light. The binding of *Leb* to *H. pylori* is well expressed for concentrations in the range between 10^3 and 10^8 *CFU/ml*: the spectral shift is in the range of 1 to *7 nm*. Interaction with 10^3 and 10^2 *CFU/ml* of *H. pylori* generates a spectral shift slightly above the measurement accuracy of the spectrometer, which is about 1 nm. The overall measurement accuracy was estimated to be approximately ± *1 nm* for amplitude measurement, while the LOD was close to 1.8 nm – Figure 3. 6 (a). Thus, a concentration of 10^2 *CFU/ml* cannot be distinguished from 10^3 *CFU/ml*. The minimum concentration of *H. pylori* with a reliably established binding to *Leb* is approximately *3000 CFU/ml*.

In phase measurement, the spectral position of the resonance is determined by the position of the inflection point in the spectral dependence of the phase jump.

In phase measurement, the overall detection accuracy was estimated to be approximately ± *0.3 nm*, while the LOD was lower than *1 nm* - Figure 3. 6 (b). Thus, statistically reliable measurements establish binding reactions at approximately *200 CFU/ml*, i.e., an improvement in LOD of about *35 %* has been achieved.

3.2 Gas sensor: hydrogen detection

In addition to the high SNR inherent in phase measurement, another key advantage is high sensitivity, i.e., the ability to measure small changes in the measured quantity. In the case of SPR sensors, this is the refractive index (*RI*) or the quantity that determines it, e.g. concentration. The high sensitivity is due to the steep spectral dependence of the phase, which we call the "phase jump". This gives us two measurement options, the second of which is alternative:

- To determine the spectral position of the inflection point of the phase jump, which corresponds to the position of resonance with much greater accuracy.
- To record large changes in the phase value for small changes in *RI* measured at a fixed wavelength (Figure 3. 7) determined by the amplitude measurement.

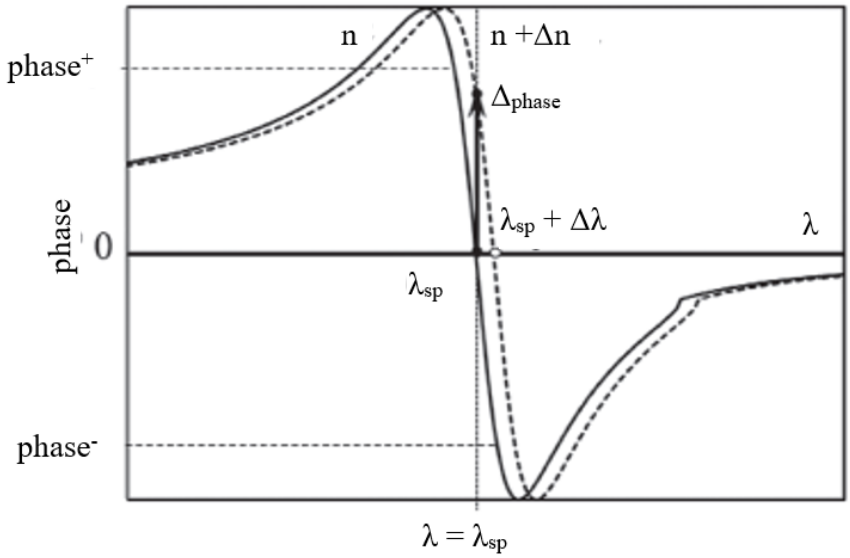

Figure 3. 7 Measurement of small Δ_{RI} with high sensitivity

Figure 3. 7 explains the principle of the alternative measurement method:

- the change Δ_{RI} determines Δ_{phase};

- the change $\Delta_{RI} \in (phase^{-}, phase^{+})$ is necessary to ensure a phase change in the linear section of the spectral dependence; outside this range, high-sensitivity measurement cannot be achieved.

The aim of the study presented below is to experimentally determine whether phase measurement provides better sensitivity than amplitude measurement, as well as to compare the two alternative phase measurements. Given the requirement $\Delta_{RI} \in (phase^{-}, phase^{+})$, the experiment requires a small and precisely controllable change in the refractive index. This can be achieved in gas detection. For this purpose, a diffraction grating-based hydrogen SPR sensor was developed.

This sensor was chosen because of the specific technological challenge associated with the widespread use and large-scale distribution of hydrogen gas — the high flammability of H2/air mixtures at H2 concentrations above *4 %.* This determines the exceptional importance of reliable and fast sensors for detecting hydrogen gas leaks.

H2 detection is performed by measuring the characteristics of Pd or WO3, which interact with H2 and whose characteristics, changed because of the interaction with H2, are measured. In our sensor, WO3 was used as the sensitive material. The interaction of H2 with WO3 is achieved through a chemical reaction in which oxygen atoms from the WO3 molecule interact with hydrogen. The reaction is completely reversible, and the relaxation time is short. The chemical reaction changes the complex refraction index of the material, which is the basis of optical detection.

Like all grating based SPR sensors, the sensitive material WO3 was deposited on a gold-plated diffraction grating. A nanostructured layer with high roughness and porosity was achieved, as shown in Figure 3. 8.

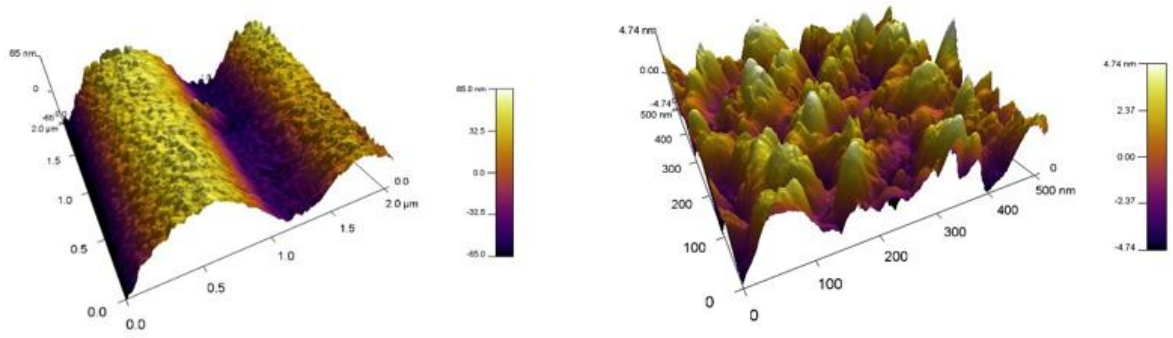

Figure 3. 8 AFM image of deposited WO3 nanostructured layer on diffraction grating

The chip thus prepared is mounted in a flow cell shown in Figure 3. 2. One channel of the cell is continuously purged with Ar, and the measured resonance is taken as a reference. The other channel is initially purged with Ar and then sequentially with different concentrations of H2, with Ar as the accompanying gas. The result of the amplitude and phase shift at *0 %* H2 (Ar only), *37.5 %* H2, and *75 %* H2 is shown in Figure 3. 9.

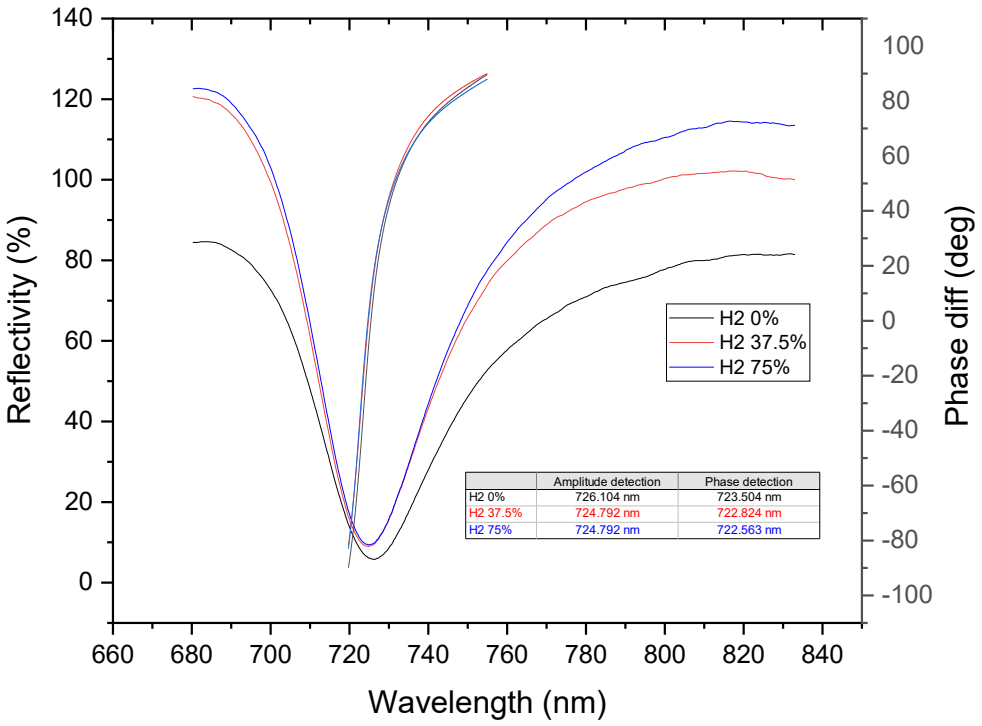

Figure 3. 9 Amplitude and phase measurement of SPR during H2 detection: 0%, 37.5%, and 75%

The spectral shifts shown in Figure 3. 10, caused by the H2/WO3 interaction at different hydrogen concentrations, were evaluated relative to the reference resonance wavelengths of Ar-blown chips. The resonance for each concentration was measured 20 times to establish the measurement error. In Figure 3. 10, the black graph shows the spectral shift of the resonance at different hydrogen concentrations, measured in phase by determining the spectral position of the inflection point; the red graph shows the same value determined by amplitude measurement.

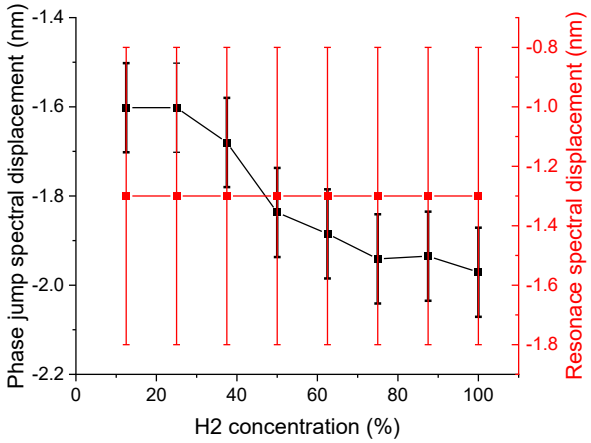

Figure 3. 10 Spectral shift of resonance as a result of H2/WO3 interaction; red curve – for amplitude measurement; black curve – for phase measurement

No hydrogen is detected during amplitude measurement: spectral shift is recorded, identical for the entire concentration range. The shift is within the margin of error, given the resolution of the spectrometer (1 nm) and the established standard deviation (0.5 nm).

In phase measurement, the established standard deviation is five times less than that of amplitude measurement (0.1 nm) due to the high steepness of the spectral dependence of the phase. This determines the statistical reliability of the measurements. Given the refractive indices of the gases (n_{Ar}=*1.0000282,* n_{H2}= *1.000263*), **the detection sensitivity is at least *1.10-5 RIU/nm***, determined as (n_{Ar} - n_{H2})/$\Delta\lambda$ at *100 %* H2. Although the concentration dependence is well expressed, concentrations up to *40 %* H2 are not statistically distinguishable, as are concentrations in the range *50 - 100%*. This is probably due to poor control of the volume ratio of the gases. A linear dependence of the refractive index of the gas mixture on the concentration can reasonably be assumed, **giving a detection sensitivity of about *2.5.10^5 nm/RIU* (*4.10^{-6} RIU/nm*)**.

The alternative phase measurement method illustrated in Figure 3. 7 was also investigated. The database is the same as in the previous study, but the difference Δ_{phase} between the reference phase (when blown with Ar) and the phases at different hydrogen concentrations was calculated. The standard deviation of the CSP was determined to be *0.2 deg*. The results are shown in Figure 3. 11.

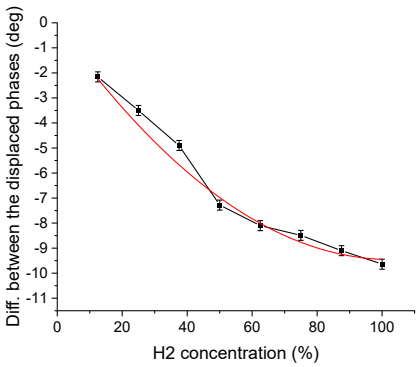

Figure 3. 11 The difference between the reference phase and the phases measured at different hydrogen concentrations

Unlike the previously described phase measurement method, here all hydrogen concentrations are statistically reliable, despite the difficulties with controlling the volume ratio of the gases. Under the same assumptions for the dependence of the refractive index of the gas mixture on concentration change, **the measured detection sensitivity is about *5.10^5 deg/RIU* (*2.10^{-6} RIU/deg*)**. It can be estimated that the sensitivity of this measurement method is three times higher than that of the alternative, although the measured values are different: *nm/RIU* or *deg/RIU*

The established sensitivity of the phase measurement method is about two orders of magnitude higher than that of the amplitude measurement. However, this is achieved with small changes in the RIU of the analyte, which is the main disadvantage of the method – the small dynamic range. To address this issue, a model experiment has been developed in which liquids with different refractive index units (RIU) are detected across a wide dynamic range, as described in detail in the dissertation.

3.3 Magneto-optical sensor (MOS)

A major advantage of MCSP is the determination of the spectral dependence of Stokes parameters from a single measurement of the amplitude-polarization modulated spectrum. This offers two advantages: fast detection and determination of the spectral dependence of all polarization characteristics of the light under investigation.

MOS are very suitable for the application of MCSP and determining its effectiveness, as they are based on the Faraday effect, and measurement is accompanied by a change in SOP. The measurable quantity is the angle of rotation of the polarization plane, which is easily determined once the Stokes parameters have been defined. It is important that the MCSP provides the spectral dependence of the Faraday rotation angle, which is necessary for accounting for temperature changes.

3.3.1 Magneto-optical effect

In MOS, magnetic field measurement is based on the linear magneto-optical effect (MOE) (Faraday effect), in which the plane of linearly polarized light rotates when it passes through a material subjected to a magnetic field in the direction of light propagation. This rotation is proportional to the magnetic field induction and the distance the light travels through the material. It is quantified by the Verdet constant, which depends on the material itself, the wavelength of the light, and the temperature. The Faraday rotation angle Θ can be expressed as:

$$\Theta = V.B.L, \tag{3.1}$$

where V is the Verdet constant, B is the magnetic induction, and L is the distance that light travels through the material.

Two main methods are used to measure the azimuth of the polarization rotation induced by the magnetic field: polarimetric and interferometric.

The simplest polarimetric scheme consists of a polarizer and an analyzer with magneto-optical materials (MOM) between them, as shown in [42]. Various signal analysis techniques are used to measure the Faraday rotation angle. In [41], a method is investigated in which Faraday rotation is converted into spectral modulation. Interferometric measurement schemes

measure the Faraday rotation angle as the phase difference between the two orthogonal circular polarizations.

MOMs are crystals or doped glasses that have a high Verdet constant and a low absorption coefficient. In the early 1990s, the Bi12SiO20 (BSO) crystal was established as a promising MOM. In addition to its high Verdet constant, BSO is not birefringent and is characterized by high optical activity. Optical activity contributes to spectral modulation but is the main cause of temperature instability in measurement.

3.3.2 MCSP applied in MOS

The study aims to establish the advantages of MCSP when applied in MOS, which would lead to improved sensitivity and measurement accuracy. This includes measurements of parameters dependent on current strength, as well as deviations of these parameters caused by temperature. For this purpose, the experimental setup is shown in Figure 3. 12 was created.

The MOM used in the experiment is a BSO crystal with dimensions (4 x 4 x 25) mm and is mounted in an aluminum holder, as shown in Figure 3. 12 and Figure 3. 13.

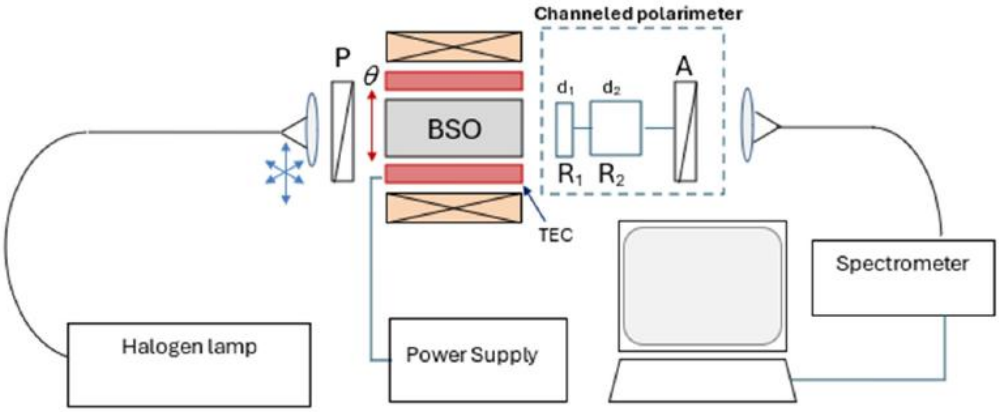

Figure 3. 12 Experimental setup of the MCP: P — polarizer; θ — angle of orientation of the polarizer; BSO—Bi12SiO20 crystal; TEC — thermoelectric coolers; R1 and R2 — birefringent quartz retarders; d1 and d2 — thicknesses of the retarders; A — analyzer

Using a thermoelectric cooler (TEC), the temperature of the crystal is changed within the range of *-32 °C* to *+62 °C* with an accuracy of *±1 °C*. A polarizer is placed in front of the crystal, through which collimated light is transmitted from a quartz-polymer optical fiber with a core diameter of *600 μm*. The light source is a white halogen lamp (Ocean Optics HL-2000, Ocean Optics, Orlando, FL, USA). The light passing through the crystal and the analyzer is focused by a collimator into a similar optical fiber connected to a spectrometer (Avantes AVASPEC-ULS2048CL-EVO, Avantes, Apeldoorn, Netherlands) with a resolution of *1 nm* and a range from *400* to *900 nm*. The BSO crystal and TEC mounted in the holder are placed in the center of a solenoid that creates a homogeneous magnetic field with an intensity of up to *700 G* along the crystal axis. The power supply provides a current *I* in the range from *-30 A* to *+30 A (±0.1 A)* to power the coil.

CSP is in a standard configuration: two birefringent retarders R_1 and R_2, with fast axis orientations of *0°* and *45°* respectively, and an analyzer A (Glan-Thompson calcite polarizer), whose transmission axis defines the reference *0°*. The BSO crystal and the CSP are in a common

construction, as shown in Figure 3. 13. If necessary, CSP is removed and replaced with analyzer 5, transforming the optical scheme into a standard polarimetric one.

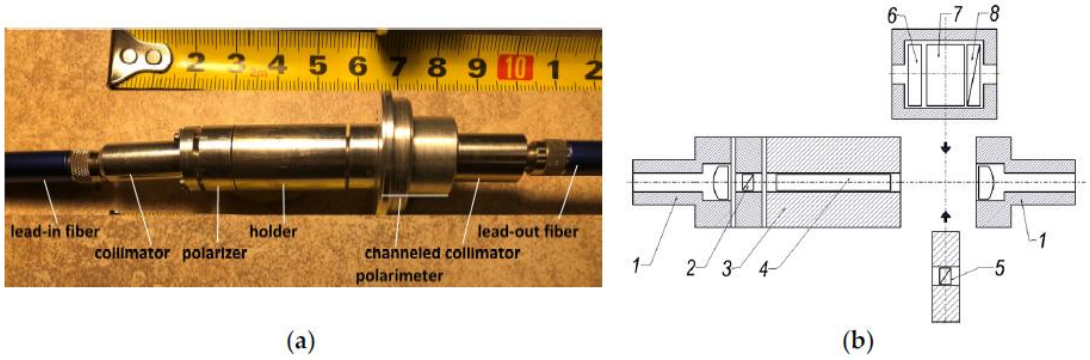

Figure 3. 13 Photo of the sensor element, including a CSP. (b) Schematic drawing of the sensor element: 1 collimators; 2 polarizer; 3 holder; 4 BSO crystal; 5 analyzer; 6, 7 - retarders with thicknesses d_1 and d_2, respectively; 8 analyzer; 6, 7, 8 constitute a CSP, which can be structurally replaced by the analyzer.

The sequence of measurements is as follows:

At a fixed temperature T between *-20 °C* and *+50 °C*, the current varies in the range from *-24 A* to *+24 A*. For each current value, the spectrum modulated by polarization interference is measured (Figure 3. 14(a)).

After scanning the currents, a new temperature value is selected, and step (a) is repeated.

The normalized values of Stokes parameters $S_1(\lambda,I)/S_0(\lambda,I)$, $S_2(\lambda,I)/S_0(\lambda,I)$ *u* $S_3(\lambda,I)/S_0(\lambda,I)$ were extracted from the stored spectra.

3.3.3 Working hypothesis

The spectral parameters of Stokes are determined from the amplitude-polarization-modulated spectrum (Figure 3. 14) using the procedure described in Section 1.3 of the dissertation. Then, the spectral dependence of the azimuth of the polarization plane is easily determined:

$$\Theta = atan2(S_2,S_1)/2, \tag{3.2}$$

where atan2 is the four-quadrant inverse tangent.

After changing the current, the new spectral dependence of the azimuth of the polarization plane is determined from the new spectrum. The difference between the two dependencies gives the angle of Faraday rotation.

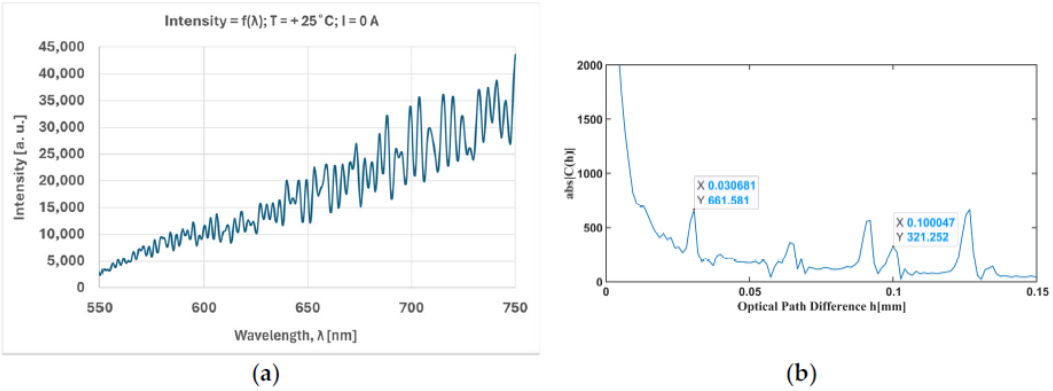

Figure 3. 14 (a) Measured spectrum modulated by polarization interference. (b) Autocorrelation function

The experimental verification of the measurement protocol was performed by measuring the intrinsic optical activity of BSO. Given the well-known data for this characteristic, we expected to obtain similar results. However, they differed dramatically. The Stokes parameters determined as a function of current did not correspond to the expected model of physical interaction. The behavior of S_3/S_0, illustrated in Figure 3. 15, is indicative.

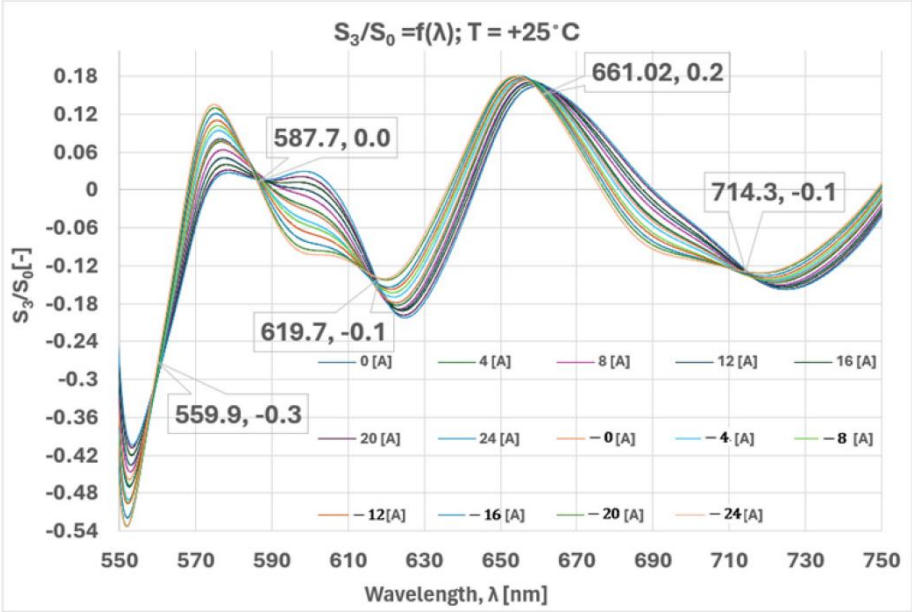

Figure 3. 15 Spectral dependence of the normalized S_3 Stokes parameter at a constant temperature of +25 °C and a current change from -24 A to +24 A

The spectral dependencies of S_2/S_0 and S_3/S_0 show well-defined, specific (locus) points at certain λ (marked in the figure above), where the SOP is approximately the same for all values of the current/magnetic field.

It is surprising that $S_3/S_0 \neq 0$, given that the input polarization is linear and that the BSO crystal is assumed to be non-birefringent, as it is an ideal circular retarder. The observed $S_3/S_0 \neq 0$ can only be explained by the presence of birefringence in the crystal due to residual stresses caused during the processing and mounting of the crystal in the holder. To illustrate this, we will discuss ellipticity and its spectral dependence.

3.3.4 Determination of SOP in MOS based on BSO

With respect to the Poincare sphere, each possible SOP can be represented by a point with two spherical angular coordinates *(2η, 2ε)*, namely length (i.e., azimuth angle) and width (i.e., ellipticity). As stated in [43], the optical rotator can produce any output SOP that has the same initial width, i.e., $\varepsilon = 0$ for the input linear polarization, as is the case with our sensor. Any polarization state with $\varepsilon \neq 0$ can be achieved by adding the effect of a linear retardation to the effect of the rotator. The phase difference introduced by the two elements in our sensor depends not only on their orientation but also on the dispersion due to the polychromatic light source. This explains the complex nature of the ellipticity shown in Figure 3. 16 and obtained from S_3/S_0:

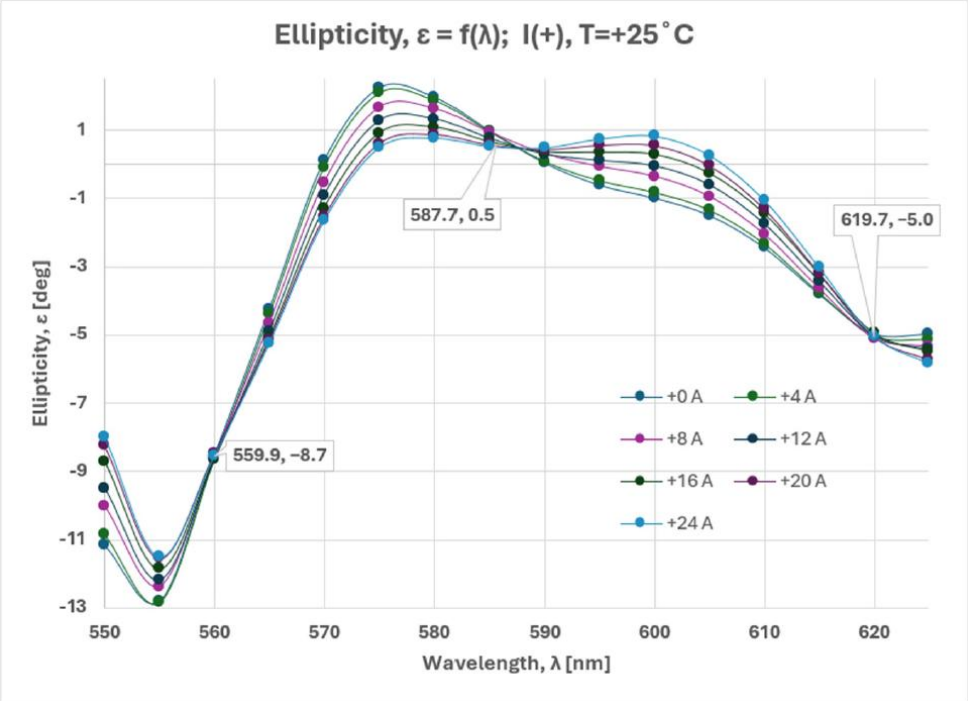

Figure 3. 16 Calculated ellipticity at varying current from +0 A to +24 A at T = +25 °C

The BSO crystal in our experiment is optically equivalent to an optical system consisting of two elements: a linear retarder and a rotator. The phase difference introduced by the optical rotator consists of the intrinsic optical activity ρ *(deg/mm)* of the BSO and the additional optical activity $\rho_F = V_B B$ caused by the Faraday effect, amplified by the crystal length L (VB and B are the Verdet constant and the magnetic field, respectively). Both the intrinsic optical activity ρ and the Verdet constant V_B depend on λ and T. The total phase difference $\Delta\Phi$ between left- and right-circularly polarized waves can be expressed as:

$$\Delta\Phi(\lambda, T) = (\Delta\Phi_{LR}(\lambda, T) + \varrho(\lambda, T) \pm V_B(\lambda, T)B)L, \tag{3.3}$$

$\Delta\Phi_{LR}(\lambda, T)$ is introduced by the linear retardation, the last two terms of the equation are the phase difference introduced by the optical rotator. The sign depends on the direction of the magnetic field: in the direction of light propagation or opposite.

3.3.5 Direct measurement of Faraday's phase difference

The surprising presence of double refraction in the BSO crystal does not explain the physical meaning of the locus points. To clarify this, the MCSP experiment described in Section 3.3.2 of the dissertation was tested on an experimental setup (Figure 3. 12) but modified – CSP was

replaced with an analyzer. In the simple polarimetric scheme thus implemented, the spectral response has the form shown in Figure 3. 17.

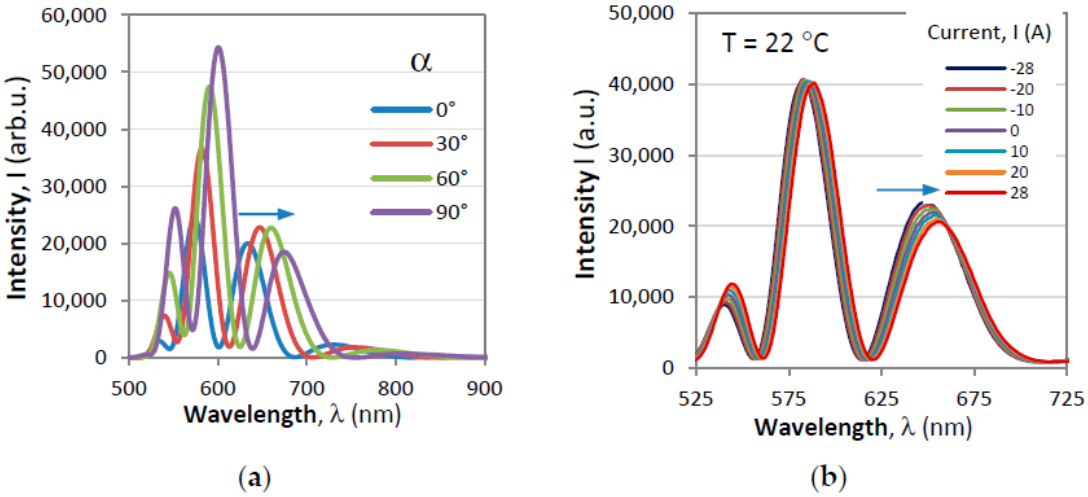

Figure 3. 17 Spectral response of the polarimetric sensor: (a) when increasing the angle of the analyzer from 0° to 90°; (b) when increasing the current in the coil from −28 A to +28 A

The information about temperature and current (magnetic field) is encoded in spectral modulation, which is why we call this measurement method the MSM (Method of Spectral Modulation) [42], [44].

The periodic modulation of the broadband spectrum of the source is caused by the dispersions of the optical activity and the Verdet constant of the BSO crystal. The intensity of the periodic modulation is determined by the expression:

$$I = \frac{1}{4} + \{1 + cos[2(\Phi + \theta - \alpha)]\}, \tag{3.4}$$

θ and α are the orientations of the polarizer and analyzer, Φ is the accumulated phase along the length of the circular birefringent BSO crystal with length L, and $\Delta\beta$ is the difference in the propagation constant between the left and right circularly polarized waves:

$$\Phi = \Delta\beta_L \tag{3.5}$$

$$\Delta\beta = \Delta\beta_L - \Delta\beta_R \tag{3.6}$$

The states of linear polarization at two adjacent maximum/minimum points are mutually perpendicular, or more precisely, the phase difference is 90^0. Figure 3. 17 (a) shows that the position of the minima/maxima can be changed by rotating the analyzer. Figure 3. 17 (b) shows that the positions of the minima/maxima depend on the magnetic field: Faraday's phase difference is introduced and the polarization plane is rotated, and due to the dispersion of the Verdet constant , the wavelengths with minimum/maximum intensity change. Based on this effect, a method for measuring magnetic field/current has been proposed [42].

Figure 3. 18 shows the polarimetric response to temperature changes in the absence of a magnetic field *($I = 0$ A)*. The polarimetric response is measured at each temperature. Since the difference $\Delta\beta$ depends on both λ and T [42], its changes manifest themselves as a shift of λ in the polarimetric response, which can be seen in Figure 3. 18.

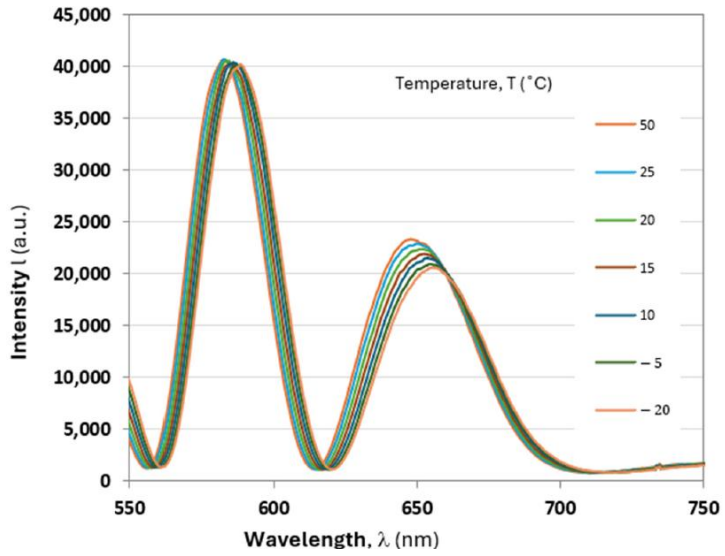

Figure 3. 18 The polarimetric response measured by MSM at I = 0 A and temperature changes from -20 °C to +50 °C

At $I_0 = 0\ A$, we can orient the analyzer so that the maximum spectral response is at 588 nm, i.e., it coincides with one of the locus points. It turns out that the other maxima/minima coincide with the remaining locus points. Since the analyzer was oriented at $I_0 = 0\ A$, the change in ellipticity due to the current (magnetic field) must be considered relative to the ellipticity at $I_0 = 0\ A$:

$$\Delta\varepsilon_n(I_n, \lambda) = \varepsilon(I_n, \lambda) - \varepsilon(I_0, \lambda) \tag{3.7}$$

These spectral dependencies are shown by the colored curves in Figure 3. 19. The locus points have zero ordinate and coincide exactly with the minima/maxima of the spectral polarimetric response shown by the black curve.

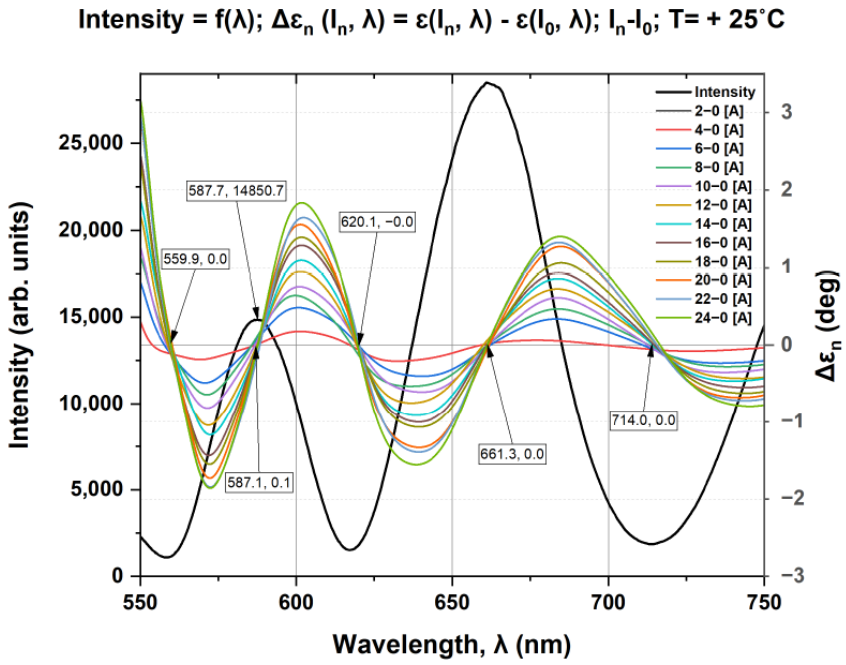

Figure 3. 19 Correlation between the zero crossing points of $\Delta_{\varepsilon n}$ (the points of the locus of S_3/S_0) and the minima/maxima of the spectral polarimetric response at +25 °C and when the current changes from 0 A to +24 A

Therefore, the phase difference introduced between two consecutive points on the locus is 90^0. Consequently, the spectral change in ellipticity is due to the phase difference between the orthogonal circularly polarized waves. Thus, the phase difference is not a consequence of the linear retarder and its own optical activity, since the term $\varepsilon(I_0, \lambda)$ in equation (3.7) accounts for their contribution. Therefore, it can be concluded that the Faraday rotator causes a phase difference in the plane $\varepsilon = const$ of the Poincare sphere, **manifested as a spectral dependence of the ellipticity**. This was observed in our experiment and corresponds to the dependence shown in Figure 3. 12 [39]. **In fact, the magnitude of the spectral dependence of the ellipticity is the phase difference caused solely by the Faraday rotation ρ_F.**

$$\Delta\varepsilon_n(I_n, \lambda) = \cos\left(V_B(\lambda, T)B_n L\right) \tag{3.8}$$

3.3.6 Magnetic field measurement

The magnetic field induced by the current can be determined from the spectrally manifested Faraday phase shift in the linear part of the dependence (3.8), around the locus point. Figure 3. 20 shows the dependence of the phase shift on the current/magnetic field for fixed λ (dotted curves) in this part of the dependence. The Verdet constant for the corresponding λ is determined from [44], [45]. The theoretical expectation according to (3.8) is shown by solid lines and is in good agreement with the experiment.

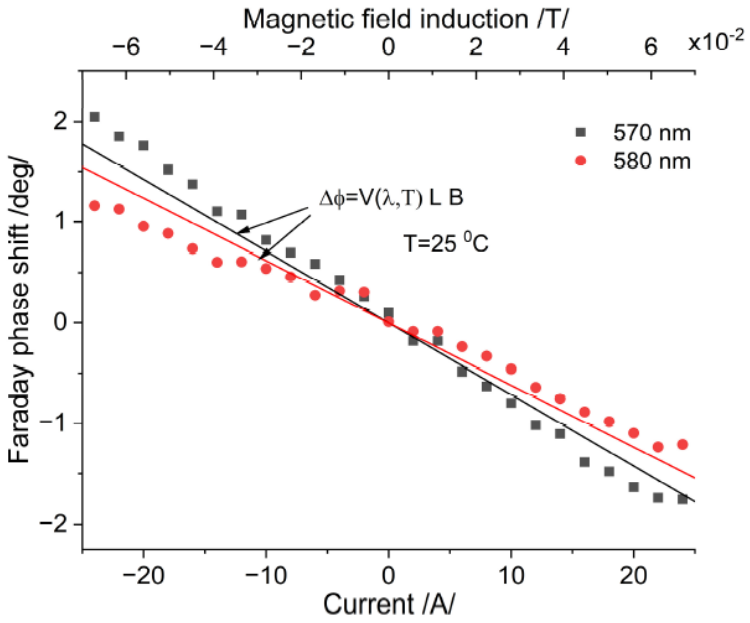

Figure 3. 20 Faraday phase shift measured by MCSP (dots) and theoretical data (solid lines)

3.3.7 Temperature stability

As shown in [46], the ellipticity and zero crossing points observed in our experiment depend on the birefringence and orientation of the polarizer. In principle, the temperature dependence of birefringence is minimal when the input polarization is parallel to the linear retarder's own axis. With this in mind, we experimentally find an orientation of the input polarization at which the spectral position of the locus points does not change by more than *0.3 %* in the temperature range from -20 *°C* to $+50$ *°C*, as shown in Figure 3. 21(a).

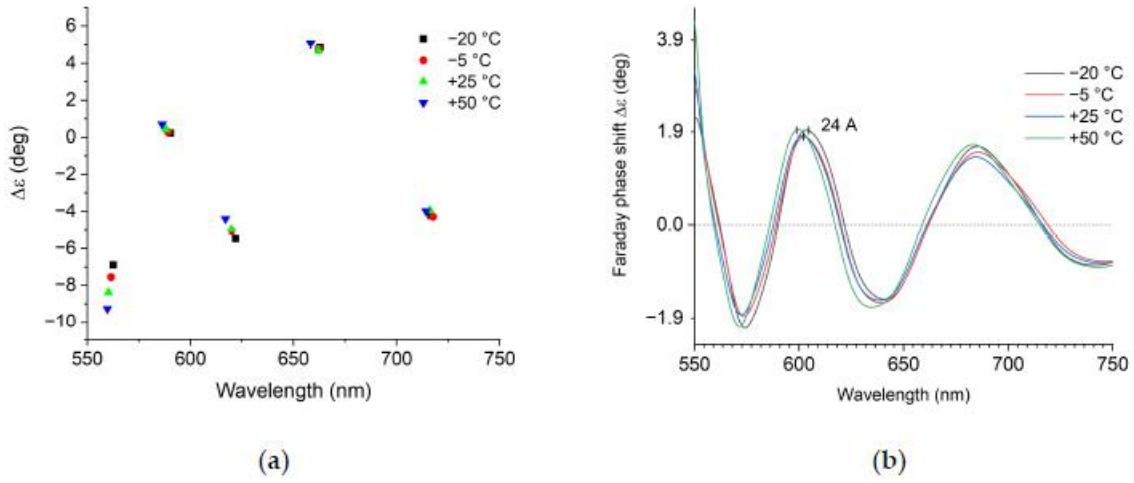

Figure 3. 21 Experimentally observed temperature stability: (a) of the spectral position of the zero-crossing points and (b) of the magnitude of the Faraday phase difference

Compared to the deviation of the extremes at different temperatures in MSM (Figure 3. 18), the temperature stability is significantly better in MCSP.

The zero-crossing points can be considered as operating points of the output SOP. Since they are independent of temperature, the phase differences that lead to spectral changes between these two points are also independent of temperature. This has been observed experimentally and is illustrated in Figure 3. 21 (b), showing the spectral dependence of the phase difference at currents of *+24 A* in the specified temperature range. The same behavior has been observed at other current values.

The magnitude of the Faraday phase difference at 602 nm is 1.9 ± 0.1^{0} (Figure 3. 21 (b)) for the entire temperature range. This means that the magnetic field measurement is practically temperature independent. This can be considered a very good achievement, given the accuracy with which the temperature of the BSO crystal is controlled ± *1 °C*.

3.3.8 Main conclusions

To our knowledge, MCSP is being applied for the first time for magnetic field/current measurement.

This method offers the unique opportunity to determine the operating point of the initial polarization state, to control its spectral position and temperature drift by **directly measuring the phase shift caused by the Faraday effect. This allows high temperature stability of measurement to be achieved, overcoming the main problem with MOS.**

Conclusions

The research conducted within the framework of the dissertation enabled the accumulation of substantial experimental expertise in the design and investigation of precise optical schemes, in which the quality of the collimated polychromatic beam was of critical importance. The design and fabrication of the CSP represented a significant challenge, which was successfully overcome, in part due to the precisely manufactured phase retarders.

Phase retarders were fabricated with pre-calculated thicknesses and ratios, ensuring that the highest-frequency modulations are spectrally resolvable. Two structural variants were implemented: with a thickness ratio of *1:2 (R1 = 4.4 mm* and *R2 = 8.8 mm)* and with a ratio of *1:3 (R1 = 3.4 mm* and *R2 = 10.2 mm)*. Their design and fabrication were based on values obtained through calculations aligned with the spectral resolution of the AvaSpec-ULS2048-CL-EVO spectrometer, which provides higher spectral resolution — *1 nm* compared to *1.4 nm* for the Ocean Optics SpectraSuit USB2000.

The fast axes of the phase plates were aligned according to Variant 3 from Table 2. 3, under which the best agreement was observed between the Stokes parameters measured with the Thorlabs polarimeter and those demodulated at the output after the CSP.

The configuration of the phase plates with a thickness ratio of *1:3 (R3.4 : R10.2)* provides higher spectral resolution in each channel, and with the presence of 9 channels — compared to the *1:2* configuration *(R4.4 : R8.8)* with *7* channels — it includes an additional channel containing information on the normalized parameters S_2 and S_3. This enables more precise calibration of the CSP and leads to more accurate extraction of the Stokes parameters.

The experimental results obtained with the biosensor for the detection of *Helicobacter pylori* demonstrate a drastically higher signal-to-noise ratio (SNR) under phase-based measurement, achieving an overall detection accuracy of approximately *±0.3 nm*, while the limit of detection (LOD) is below *1 nm*, as shown in Figure 3. 6 (b). Statistically valid measurements indicate the presence of binding reactions at concentrations around *200 CFU/ml*, corresponding to an improvement in the LOD of approximately *35 %.*

In gas sensors, phase-based measurement exhibits a standard deviation approximately five times lower than that of amplitude-based measurement (*0.1 nm*), which is attributed to the steep spectral dependence of the phase. This ensures the statistical reliability of the conducted measurements. Considering the refractive indices of the gases (n_{Ar} = *1.0000282,* n_{H_2} = *1.000263*), the detection sensitivity can be estimated at no less than $1.1 \cdot 10^{-5}$ *RIU/nm*, defined as $(n_{Ar} - n_{H_2})/\Delta\lambda$ at a concentration of *100 % H2*. Despite the clearly expressed concentration dependence, concentrations up to *40 % H2* and within the range of *50 – 100 %* do not exhibit statistically significant differences due to insufficient control over the volumetric ratio of the gases. Assuming a linear dependence of the refractive index on concentration, the detection sensitivity is estimated at approximately $2.5 \cdot 10^{5}$ *nm/RIU* ($4 \cdot 10^{-6}$ *RIU/nm)* (Figure 3. 10).

An alternative method for measuring the phase difference was applied, in which the same experimental data were used, but the phase variation was recorded as a function of changes in the refractive index at a fixed wavelength. This approach provided statistically reliable results for all hydrogen concentrations despite the difficulties in controlling the

volumetric ratio of the gases. Assuming a linear dependence of the refractive index on concentration, a sensitivity of approximately *5·10⁵ deg/RIU (2·10⁻⁶ RIU/deg)* was established (Figure 3. 11), which is about three times higher than that obtained with the alternative method, although the measured quantities differ — *nm/RIU* versus *deg/RIU*.

To evaluate the sensitivity of phase-based measurement under conditions of a large dynamic range of the refractive index, a model experiment was conducted. The aim was to determine the extent to which phase measurement provides an advantage in cases of significant variations in the refractive index. Measurements were performed using diffraction gratings with different periods, integrated into a flow cell with model aqueous solutions, in which the refractive index varied within the range of *1.33–1.35*. The results for gratings with periods of *300 nm* and *900 nm* (Figure 49 of the dissertation) demonstrated that the sensitivity of phase measurement was on average about *25 %* higher compared to amplitude measurement, while in this case the dynamic range was five orders of magnitude greater than in the experiments for H2 detection.

The channeled polarimetry method was also applied in magneto-optical sensors based on the Faraday effect. To the best of our knowledge, channeled polarimetry is being employed for the first time in the measurement of magnetic field and current. The method provides a unique opportunity to determine the operating point of the output polarization state, to control its spectral position and thermal drift, as well as to directly measure the phase shift induced by the Faraday effect. In this way, high thermal stability of the measurements is ensured, thereby overcoming the principal limitation of magneto-optical sensors.

In summary, the measurements of the spectral dependence of phase variation in sensors, where the measurement is associated with changes in the state of polarization, demonstrated the effectiveness of the CSMP through the achieved high sensitivity and signal-to-noise ratio.

This defines the future directions of research: refinement of the algorithm for processing experimental data, miniaturization of the design, optimization of the diffraction grating parameters, applications for ultra-sensitive detection of biomolecular interactions, and implementation in the measurement of other physical quantities.

Main contributions

1. The method of channeled spectrum polarimetry has been experimentally developed, which includes:
- design and manufacture of a channeled spectropolarimeter with optimal parameters of the structural elements, in line with the accompanying measuring equipment;
- established measurement accuracy and resolution.
2. The effectiveness of the method of channeled spectrum polarimetry has been experimentally proven:

- in SPR biosensors for the detection of *Helicobacter Pylori*, where a reduction in the lower detection limit of about *35 %* was recorded due to improved signal to noise ratio;

- in SPR gas sensors for hydrogen detection, where sensitivity two orders of magnitude higher than that of conventional amplitude measurement were achieved in a small dynamic range;

- in model experiments in a large dynamic range, the improvement in sensitivity is about *25 %* of that in conventional amplitude measurement.

3. The CSMP (Channeled Spectral Polarimetry Method) has been applied for the first time to magneto-optic sensors based on BSO, enabling temperature-independent direct measurement of the phase difference generated by the Faraday effect. The validity of CSMP has been confirmed through the developed MSM (Method of Spectral Modulation), which was applied for magnetic-field measurement.

ACKNOWLEDGMENTS

We would like to express our gratitude for the financial support provided by the National Science Fund through projects: КП-06/1 China, 2020, КП-06-Н48/2 26.11.2020, ПН33/1 from 2019, КП-06-78/9 from 2022, as well as the financial support from the National Center for Biomedical Photonics through agreements ДО-1/183, ДО1-352 funded by the Ministry of Education and Science. This dissertation fulfills part of the tasks included in the listed projects/agreements.

List of figures

List of publications included in the dissertation and their citations

1. A simple fiber optic magnetic field and current sensor with spectral interrogation, *T. Eftimov, G. Dyankov,* ***P. Kolev****, V. Vladev, Optics Comminication,* Volume 527, **2023**, 128930, ISSN 0030-4018, https://doi.org/10.1016/j.optcom.2022.128930

Citations:

1.1 Ma, Qianyue & Sang, Mei & Wang, Yupeng & Yang, Qingrui & Zheng, Xiaomei & Jiang, Junfeng & Cheng, Zhenzhou & Han, Qun. (2025). Development of a High-Precision Demodulation System for Fiber-Optic Current Sensors. 1-3. 10.1109/ICOCN67308.2025.11145501.

1.2 Bai, Ru & Li, Boyan & Tu, Jiakun & Yang, Tengda & Dou, Aiyu & Sun, Yucheng & Qian, Zhenghong. (2024). Dual-range TMR current sensor based on magnetic shunt/aggregation effects utilizing single magnetic ring structure. Measurement Science and Technology. 35. 10.1088/1361-6501/ad457a.

1.3 Jiao, Xinbing & Bao, Shiyi & Li, Shumin. (2023). Dynamic Responses of Garnet-Type Optical AC Sensor Based on Faraday Effect. IEEE Sensors Journal. 23. 18092-18098. 10.1109/JSEN.2023.3287472.

1.4 Dejband, Erfan & Yao, Cheng-Kai & Manie, Yibeltal Chanie & Huang, Po-Yang & Lee, Hao-Kuan & Peng, Peng-Chun. (2022). Utilizing a Tunable Delay Line Interferometer to Improve the Sensing Accuracy of an FBG Sensor System. Photonics. 9. 869. 10.3390/photonics9110869.

1.5 Kumar, Ashish & Baac, Hyoung. (2025). Recent advances and applications on fiber-optic scalar and vector magnetometers. Applied Physics Reviews. 12. 10.1063/5.0222078.

1.6 Sutanto, Erwin & Escrivá, Guillermo & Rusydi, Febdian & Yasin, Moh. (2023). Fiber Optic Based Leakage Current Measurement and its Possible Length to Achieve the Safety Limit. 1-5. 10.1109/ICWT58823.2023.10335288.

1.7 Wen, Hsin-Yi & Hsu, Yi-Ting. (2023). The Nanosilver Imprinted Cross-Channel Film used in Microfluidic Chips Based on Microcavity Resonator for Mercury Assessment. Advanced Sensor Research. 3. 10.1002/adsr.202300133.

1.8 Li, Shenwang & Huang, Shuqing & Su, Qiuren & Wu, Thomas & Zhang, Dongdong & Guo, Pinghui & Cai, Yiming. (2023). Anti-crosstalk magnetic field method for straight-light path type optical current transducer based on the background of gas-insulated substation. Optical Engineering. 62. 10.1117/1.OE.62.4.044104.

1.9 Yan, Xin & Wei, Luo & Fu, Rao & Cheng, Tonglei. (2022). Highly sensitive temperature sensor based upon a multimode interference structure filled with an ethanol-glycerol solution. Instrumentation Science & Technology. 51. 1-13. 10.1080/10739149.2022.2158195.

2. A Spectrally Interrogated Polarimetric Optical Fiber Sensors for Current Measurement with Temperature Correction, T. Eftimov, G. Dyankov, **P. Kolev**, V. Vladev, L. Kolaklieva, Sensors, **2023**, *23*(23), 9306; **https://doi.org/10.3390/s23239306**

3. Biosensor-based serological assay for diagnosing Helicobacter pylori infection, ***P. Kolev****, G. Dyankov, E. Hikova, H. Kisov,* ***2024*** *IOP Conf. Ser.: Earth Environ. Sci.* ***1305*** *012019,* ***DOI*** *10.1088/1755-1315/1305/1/012019*

Citations:

3.1 Lutomia, Desmond & Poria, Rachna & Kala, Deepak & Singh, Anupam & Gupta, Manoj & Kumar, Deepak & Kaushal, Ankur & Gupta, Shagun. (2024). Unlocking the potential of 2D nanomaterial-based biosensors in biomarker-based detection of Helicobacter pylori. Materials Advances. 6. 117-142. 10.1039/D4MA00546E.

4. Channeled polarimetry for magnetic field/current detection**,** G. Dyankov, **P. Kolev**, T. Eftimov, E. Hikova, H. Kisov, Sensors, **2025**, *25*(2), 466; **https://doi.org/10.3390/s25020466**

Citations:

4.1 Chen, Wei & Chen, Huaijie & Xu, Haibo & Li, Li. (2025). Design and Characterization of a Self-Oscillating Fluxgate-Based Current Sensor for DC Distribution System Applications. Sensors. 25. 2360. 10.3390/s25082360.

List of participations in scientific forums

Oral presentations:

1. Application of spectral polarimetry in surface plasmon resonance-based biosensors, 17th Spring Seminar on Interdisciplinary Chemistry, (Sofia, Bulgaria, April 23-25, 2024)

Poster presentations:

1. Kolev P, Dyankov G and Eftimov T, **Spectral polarimetry applied for magnetic field detection,** *22th International School and Conference on Condensed Matter Physics* (Varna, Bulgaria, 29 august – 2 september 2022).

2. Kolev P and Zhao B, **Spectral polarimetry method,** *4th Interdisciplinary PhD Forum with International Participation* (Sandanski, Bulgaria, 16 – 19 may 2023).

3. Kolev P, Hikova E and Dyankov G, **Serological assay for diagnosing Helicobacter pylori infection performed by biosensor,** *International Conference Kliment's Days 2023 - 60 Years Faculty of Biology* (Sofia, Bulgaria, 9-10 november 2023).

4. Kolev P, Dyankov G, Eftimov T, **Spectrally modulated polarimetry for magnetic field measurement,** *4th national congress on physical sciences* (Sofia, Bulgaria, october 7-9 2024).

5. Hikova E, Kolev P, Veselinov P, Dyankov G, Genova-Kalou P, **Rapid detection of pesticides via surface plasmon resonance (SPR) method,** 16th Scientific Conference of the Bulgarian Contact Point of EFSA at the Center for Risk Assessment in the Food Chain (Sofia, Bulgaria, May 16, 2024).

6. Kolev P, **Spectral polarimetry detection of surface plasmon resonance,** *5th Interdisciplinary PhD Forum with International Participation* (Kyustendil, Bulgaria, 16-19 April 2024).

7. Dyankov G, Kereziev T, Genova-Kalu P, Kolev P, Veselinov P, Hikova E, Kisov H, **Wavelength interrogated grating-based SPR sensor operating in 1.8 –2.2 µm range**, *11th International Conference on Surface Plasmon Photonics* (Tokyo, Japan, 19-23 may 2025).
8. Kolev P, Eftimov T, Hikova E, Veselinov P, Kisov H, Dyankov G, **Direct detection of Faraday phase shift in magneto-optical materials**, *International Conference of Advances in Materials Science & Photonics* (Bansko, Bulgaria, 15-18 july 2025).

Bibliography

[1] B. L. T. L. C. Nylander, "Gas detection by means of surface plasmons resonance," *Sensors and Actuators,* vol. 3, p. 79–88, 1982.

[2] J. S. J. G. M. P. I. Pockrand, "Surface plasmon spectroscopy of organic monolayer assemblies," *Surface Sci.,* vol. 74, p. 237–244, 1978.

[3] R. G. K.A. Peterlinz, "Two-color approach for determination of thickness and dielectric constant of thin films using surface plasmon resonance," *Opt. Commun.,* vol. 130, p. 260–266, 1996.

[4] I. L. E. S. B. Liedberg, "Principles of biosensing with an extended coupling matrix and surface plasmon resonance," *Sensors and Actuators B,* vol. 11, p. 63–72, 1993.

[5] D. U. L.M. Zhang, "Optical chemical sensing employing surface plasmon resonance," *Electron. Lett.,* vol. 23, p. 1469–1470, 1988.

[6] A. B. G. G. Ch. Striebel, "Characterization of biomembranes by spectral elipsometry, surface plasmon resonance and interferometry with regard to biosensor application," *Biosens. Bioelectron.,* vol. 9, pp. 139-146, 1994.

[7] R. B. C. L. D.C. Cullen, "Detection of immunocomplex formation via surface plasmon resonance on gold coated diffraction gratings," *Biosensors,* vol. 3, p. 211–225, 1987:88.

[8] G. B. P. C. J. S. M.J. Jory, "A surfaceplasmon- based optical sensor using acousto-optics," *Measurement Sci. Technol.,* vol. 6, p. 1193–1200, 1995.

[9] N. G. D. F. J. S. C.R. Lawrence, "Surface plasmon resonance studies of immunoreactions utilizing disposable diffraction gratings," *Biosens. Bioelectron.,* vol. 11, p. 389–400, 1996.

[10] S. L. e. al, "Grating coupled SPR sensors using off the shelf compact discs and sensitivity dependence on grating period," *Sensors and Actuators Reports,* 2020.

[11] Y. S. H. Z. M. C. X. Z. S. G. J. Cao, "Plasmon-enhanced optical transmission at multiple wavelengths through an asymmetric corrugated thin silver film," *Plasmonics,* vol. 13, p. 1549–1554, 2018.

[12] H. G. S. R. M. T. Khaleque, "Fabrication of resonant patterns using thermal nanoimprint lithography for thin film photovoltaic applications," *Opt. Express,* vol. 21, p. A631–AA41, 2013.

[13] S. W. A. M. T. H. Y. C. A. M. e. a. N. Pourdavoud, "Photonic nanostructures patterned by thermal nanoimprint directly into organo-metal halide perovskites," *Adv. Mater. ,* vol. 29, p. 1605003, 2017.

[14] P. L. P. N. E. M. G. A. V. F. H. A. P. D. L. Voronov, "X-ray diffraction gratings : precise control of ultra-low blaze angle via anisotropic wetetching," *Appl. Phys. Lett. ,* vol. 109, p. 043112, 2016.

[15] H. G. O. S. K. G. M. B. A. D. B. Kaplan, "Tuning optical discs for plasmonic applications," *Plasmonics,* vol. 4, p. 237–243, 2009.

[16] B. M. P. P. -.. C. P. J. X. Dou, "High surface plasmon resonance sensitivity enabled by optical disks," *Opt. Lett.,* vol. 37, p. 3681–3683, 2012.

[17] A. K. A. S. M. A. I. A. O. Krasnykov, "Sensor with increased sensitivity based on enhanced optical transmission in the infrared," *Opt. Commun.,* vol. 284, p. 1435–1438, 2011.

[18] O. K. M. A. B. H. A. G. I. A. A. Karabchevsky, "Theoretical and experimental investigation of enhanced transmission through periodic metal nanoslits for sensing in water environment," *Plasmonics,* vol. 4, p. 281, 2009.

[19] B. M. P. P. -.. C. P. J. X. Dou, "High surface plasmon resonance sensitivity enabled by optical disks," *Opt. Lett.,* vol. 37, p. 3681–3683, 2012.

[20] H. Z. W. Z. A. A. H. L. L. L. e. a. Y. Liang, „Subradiant dipolar interactions in plasmonic nanoring resonator array for integrated label-free biosensing,“ *ACS Sens.,* том 2, p. 1796–1804, 2017.

[21] A. K. S. a. A. K. Pandey, "Metal oxide grating based plasmonic refractive index sensor with Si layer in optical communication band," *IEEE Sensors J.,* vol. 20, no. 3, p. 1275–1282, 2020.

[22] A. S. a. I. A. A. Lahav, *J. Nanophotonics,* vol. 3, no. 031501, 2009.

[23] S. Nelson, K. Johnston and S. Yee, "High sensitivity surface plasmon resonace sensor based on phase detection," *Sens. Actuators B Chem.,* vol. 35, p. 87–191, 1996.

[24] S. Shen, T. Liu and J. Guo, "Optical phase-shift detection of surface plasmon resonance," *Appl. Opt.,* vol. 37, p. 1747–1751, 1998.

[25] A. Kabashin, V. Kochergin, A. Beloglazov and P. Nikitin, "Phase-polarisation contrast for surface plasmon resonance biosensors," *Biosens. Bioelectron.,* vol. 13, p. 1263–1269, 1998.

[26] a. P. I. N. A.V. Kabashin, *Quantum Electron.,* vol. 27 (7), p. 653–654, 1997.

[27] a. P. I. N. A.V. Kabashin, *Opt. Commun.,* vol. 150, pp. 5-8, 1998.

[28] X. Yu, D. Wang, X. Wei, X. Ding, L. Wei and X. Zhao, "A surface plasmon resonance imaging interferometry for protein micro-array detection.," *Sens. Actuators B Chem.,* vol. 108, p. 765–771, 2005.

[29] A. Grigorenko, M. Polini and K. Novoselov, "Graphene plasmonics.," *Nat. Photonics,* vol. 6, p. 749–758, 2012.

[30] S. Ng, C. Wu, S. Wu, H. Ho and S. Kong, "Differential spectral phase interferometry for wide dynamic range surface plasmon resonance biosensing," *Biosens. Bioelectron.,* vol. 26, p. 593–1598, 2010.

[31] W. Law, P. Markowicz, K. Yong, I. Roy, A. Baev, S. Patskovsky, A. Kabashin, H. Ho and P. Prasad, "Wide dynamic range phase-sensitive surface plasmon resonance biosensor based on measuring the modulation harmonics," *Biosens. Bioelectron.,* vol. 23, p. 627–632, 2007.

[32] Y. Huang, H. Ho, S. Wu, S. Kong, W. Wong and P. Shum, "Phase sensitive SPR sensor for wide dynamic range detection," *Opt. Lett.,* vol. 36, p. 4092–4094, 2011.

[33] M. Somekh, G. Stabler, S. Liu, J. Zhang and C. See, "Wide-field high-resolution surface-plasmon interference microscopy," *Opt. Lett.,* vol. 34, p. 3110–3112, 2009.

[34] J. Gerber, S. Berweger, B. O'Callahan and M. Raschke, "Phase-resolved surface plasmon interferometry of graphene," *Phys. Rev. Lett.,* vol. 113, p. 55502, 2014.

[35] B. Sepúlveda, D. Sánchez, M. Moreno, F. Blanco, K. Mayora, C. Domínguez and L. Lechuga, "Optical biosensor microsystems based on the integration of highly sensitive Mach Zehnder interferometer devices," *J. Opt. A Pure Appl. Opt.,* vol. 8, p. S561–S566, 2006.

[36] J. Ahn, T. Seong, W. Kim, T. Lee, I. Kim and K. Lee, "Fiber-optic waveguide coupled surface plasmon resonance sensor," *Opt. Express,* vol. 20, p. 21729–21738, 2012.

[37] Y. Liu, Q. Liu, S. Chen, F. Cheng, H. Wang and W. Peng, "Surface Plasmon Resonance Biosensor Based on Smart Phone Platforms," *Sci. Rep.,* vol. 5, p. 12864, 2015.

[38] K. O. a. T. Kato, "Spectroscopic polarimetry with a channeled spectrum," *Opt. Lett.,* vol. 24, no. 21, p. 1475–1477, 1999.

[39] N. Hagen, "Design of channeled spectropolarimeters," *Appl. Opt.,* vol. 61, pp. 3381-3389, 2012.

[40] a. N. C. B. Luis Oscar Gonzalez-Siu, "Error analysis of channeled Stokes polarimeters," *Applied Optics,* vol. 60, no. 16, p. 4511, 2021.

[41] G. T. E. E. H. H. N. V. K. P. G.-K. V. M. e. a. Dyankov, "SPR and double resonance LPG biosensors for Helicobacter pylori BabA antigen detection," *Sensors,* vol. 7, p. 2118, 2024.

[42] T. Eftimov, G. Dyankov, P. Kolev and V. Vladev, "A simple fiber optic magnetic field and current sensor with spectral interrogation," *Opt. Commun.,* vol. 527, p. 128930, 2023.

[43] A. Weidner, "The Poincare sphere: Isolated and real trajectories describing the state of polarization," *J. Opt..*

[44] T. Eftimov, G. Dyankov, P. Kolev and V. Vladev, "A Spectrally interrogated polarimetric optical fiber sensor for current measurement with temperature correction," *Sensors,* vol. 23, p. 9306, 2023.

[45] P. Petkova and P. Vasilev, "Magneto-optical properties of Bi12SiO20: Ni.," *Optik,* vol. 127, p. 9076–9080, 2016.

[46] S. Petricevic and P. Mihailovic, "Compensation of Verdet constant temperature dependence by crystal core temperature measurement," *Sensors,* vol. 16, p. 1627, 2016.